Pergamon

Int. J. Solids Structures Vol. 34, No. 27, pp. 3541–3570, 1997
Published by Elsevier Science Ltd

0020-7683/97 $17.00 + .00

PII: S0020-7683(96)00210-7

APPLICATION OF A TOTAL LAGRANGIAN COROTATIONAL FINITE ELEMENT SCHEME TO INFLATION OF A TIRE

JAMES M. GREER, JR
Program Manager, Precision Airdrop, Wright Laboratories/FIVMB, Wright-Patterson Air Force Base, OH 45433, U.S.A.

ANTHONY N. PALAZOTTO
Professor of Aeronautical Engineering, Dept. of Aeronautics and Astronautics (AFIT/ENY), Air Force Institute of Technology, Wright-Patterson Air Force Base, OH 45433-6583, U.S.A.

(*Received* 30 *January* 1996; *in revised form* 15 *August* 1996)

Abstract—The aircraft tire may be treated as a composite shell, owing to its nylon-corded rubber ply construction. However, its construction is complex: the ply orientation angles, numbers of plys, ply thicknesses, and even the ply moduli change in the meridional direction (the direction perpendicular to the "rolling" direction). Moreover, the moduli of the materials used in construction span several orders of magnitude (isotropic rubber tread, nylon-corded rubber plys, steel bead wires). These features present a formidable challenge to the use of two-dimensional finite element codes when representing the behavior in individual plys is desired. In the current work, quasi-three-dimensional behavior of the tire, including transverse shear warping and thickness stretching, is generated through the finite element technique. The technique is based on the Jaumann stress measures, using a local and layer-wise displacement field to describe the behavior of the shell away from the reference surface. In contrast to stress-resultant models, this technique allows estimation of stresses and strains in individual plys, including interlaminar shear and peeling stresses. Published by Elsevier Science Ltd

1. INTRODUCTION

Classical plate and shell theory assumptions, in which it is assumed that normals to the reference surface remain straight, normal, and of unchanged length after deformation have proven inadequate for composites owing to the large ratio of elastic modulus to shear modulus of these materials. An adequate theory must account for transverse shear strains (Reddy 1984) and, in some cases, for thickness stretching.

In the current work, large displacement and large rotation analyses are undertaken using a local layer-wise assumed displacement field for modeling transverse behavior (Pai and Nayfeh 1992). Theories based upon layer-wise 2-D assumed displacement fields provide background for the present work (Epstein and Glockner, 1977; Epstein and Huttelmaier, 1983; Murakami, 1984; Hinrichsen and Palazotto, 1986; Reddy, 1989). The current work differs most significantly from the cited works in including the transverse normal strain and stress, and in directly imposing transverse shear and normal stress continuity at ply interfaces.

The current research depends upon decomposing the displacement field into a stretch and a rigid body rotation, and measuring the strains along three mutually perpendicular axes, the directions of which correspond to the rigid rotation of an orthonormal triad associated with the undeformed geometry. The (local) stresses and strains measured with respect to the newly oriented triad may be considered local engineering measures, in that material properties garnered from tensile coupon tests may be immediately introduced into the constitutive relations without transformation. These local measures are the Jaumann measures (Fraeijs de Veubeke, 1972; Atluri and Murakawa, 1977; Atluri, 1984; Danielson and Hodges, 1987), which are resolved along the rigidly displaced and rotated axes. These measures are local, geometric, directional, and work-conjugate (Pai and Nayfeh, 1994).

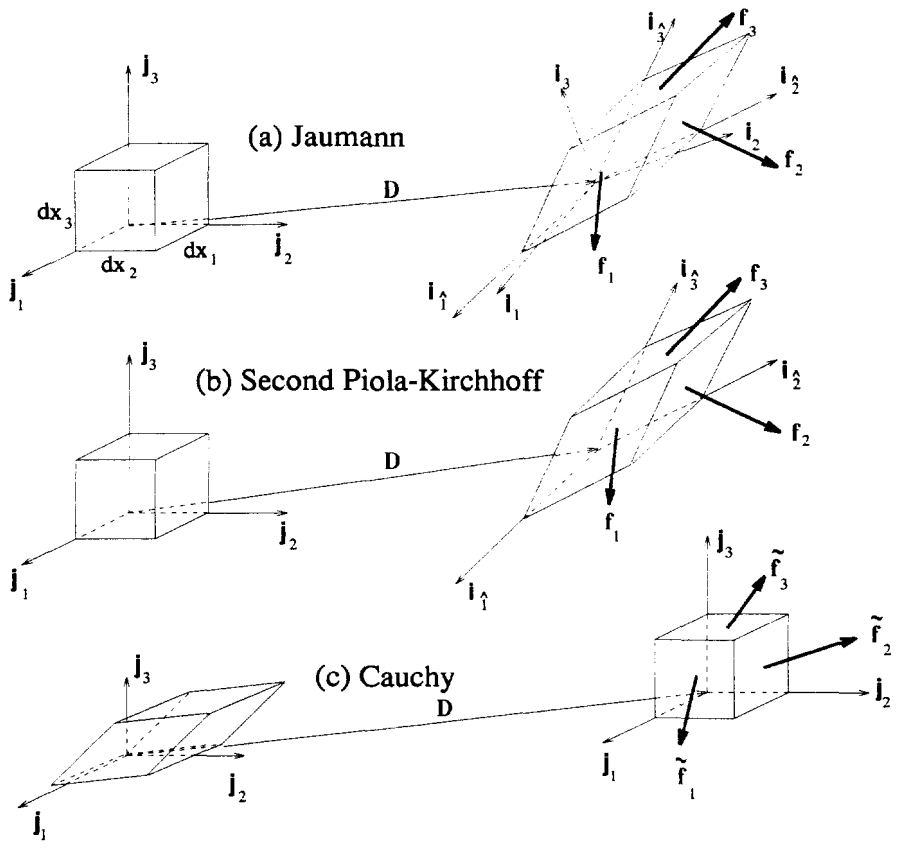

Fig. 1. Deformation of an infinitesimal volume element.

2. THEORY

The theory presented in this section is chiefly that of Pai and Palazotto (1995a). The theory makes use of the polar decomposition method to facilitate the use of a local (and linear) displacement field at an infinitesimal region of interest in the nonlinearly deforming body. In the interest of completeness, a brief overview of the theory is presented here.

The Jaumann stress J_{mn} and strain B_{mn} are given by (Pai and Palazotto, 1995a)

$$J_{mn} = \frac{1}{2\,\mathrm{d}x_1\,\mathrm{d}x_2\,\mathrm{d}x_3}(\mathrm{d}x_m\mathbf{f}_m\cdot\mathbf{i}_n + \mathrm{d}x_n\mathbf{f}_m\cdot\mathbf{i}_m) \tag{1a}$$

$$B_{mn} = \frac{1}{2}\left(\frac{\partial\mathbf{u}}{\partial x^m}\cdot\mathbf{i}_n + \frac{\partial\mathbf{u}}{\partial x^n}\cdot\mathbf{i}_m\right) \tag{1b}$$

where the $\mathbf{f}_m$ are the force resultants on the faces of the deformed parallelepiped (Fig. 1). For example, $\mathbf{f}_1$ acts on the deformed $\mathrm{d}x_2$–$\mathrm{d}x_3$ plane. The local displacement vector $\mathbf{u}$ of eqn (1b) is measured with respect to the *displaced* location of a material point, hence at any given point on the deformed reference surface, $\mathbf{u} = 0$, though its derivatives (which will give rise to the strains) are non-zero. As can be seen from eqn (1b), the Jaumann stresses and strains are defined with respect to the orthogonal directions, denoted by unit vectors $\mathbf{i}_k$, associated with the stretched and rigidly rotated volume element (Fig. 1(a)). In addition, these stress measures are associated with *undeformed* cross-sectional areas.

On the other hand, the second Piola–Kirchhoff stresses S_{mn} and Green's strain L_{mn} are defined by (Pai and Palazotto, 1995a)

$$\frac{1}{\mathrm{d}x_1\,\mathrm{d}x_2\,\mathrm{d}x_3}\mathrm{d}x_{(m)}\mathbf{f}_{(m)} = \sum_{n=1}^{3}(S_{m(n)}\lambda_n\mathbf{i}_{(\hat{n})}) \tag{2a}$$

$$L_{mn} = \tfrac{1}{2}(\lambda_{(m)}\mathbf{i}_{(\hat{m})}\cdot\lambda_{(n)}\mathbf{i}_{(\hat{n})} - \delta_{mn}) \tag{2b}$$

where λ_n is the magnitude of the so-called "lattice vector" (Washizu, 1982), and the parentheses suspend the tensor summing convention. In the figure, it is seen that the second-Piola/Green measures are associated with the directions along the deformed (and, in general, not orthogonal) edges of the element, as shown in Fig. 1(b). The directions of the lattice vectors correspond to the directions of the unit vectors $\mathbf{i}_{\hat{k}}$ (note the circumflex on the subscript). So, in general, the components of the second-Piola stresses are along neither those of the undeformed coordinate system, as are the Cauchy measures depicted in Fig. 1(c), nor those of its rigidly translated and rotated counterpart in the deformed body (as are the Jaumann measures). This is a consequence of the Green strains being energy-related measures (dealing with the change in *squared* length of a fiber) rather than strictly geometric measures, like Jaumann or engineering strains. To use the Jaumann measures, which are local, the effect of rigid body translation and rotation must be removed so that only the effect of stretching (the source of elastic strain energy) is seen. The means to perform this are now shown in an example using the *polar decomposition method*, which explicitly performs this separation of rigid body and stretching movements, allowing eqn (1b) to be formed very quickly. According to Malvern (1969):

> "The fact that the deformation at a point may be considered as the result of a translation followed by a rotation of the principle axes of strain, and stretches along the principal axes, was apparently recognized by Thomson and Tait in 1867, but first explicitly stated by Love in 1892."

By way of the polar decomposition, the Green and Jaumann strain measures are now compared and contrasted using the following (two-dimensional) global displacement field:

$$u_1 = atx_1x_2, \quad u_2 = btx_2 \tag{3}$$

where the u_i are components of displacement, the x_i are the global coordinates of an undeformed point in the body, a and b are constants, and t represents time. The coordinates (y_1, y_2) for a material point, originally located at (x_1, x_2), may then be written as

$$y_1 = x_1 + u_1, \quad y_2 = x_2 + u_2. \tag{4}$$

The deformation gradient tensor [**F**] is given by

$$[\mathbf{F}] = \mathbf{i}_k \cdot \frac{\partial \vec{\mathbf{r}}_\alpha}{\partial x_m} = \frac{\partial y_k}{\partial x_m} = \begin{bmatrix} 1+atx_2 & atx_1 \\ 0 & 1+bt \end{bmatrix}, \tag{5}$$

where $\mathbf{r}_\alpha$ is the position vector to the coordinates (y_1, y_2) associated with the displaced location. The polar decomposition (here the decomposition is discussed in the context of rectangular Cartesian coordinates, but the decomposition may be performed in curvilinear coordinates as well (see, e.g., Pai and Palazotto (1995b))) is now employed. The deformation gradient tensor may be decomposed into the product of two tensors, [**R**] and [**U**], where [**R**] describes the rigid rotation of the body at a material point, and [**U**] describes the material deformation (stretching) at that point:

$$[\mathbf{F}] = [\mathbf{R}][\mathbf{U}]. \tag{6}$$

These matrices have some special properties. The matrix [**R**] is an orthogonal rotation matrix, that is

$$[\mathbf{R}]^{\mathrm{T}}[\mathbf{R}] = [\mathbf{I}], \tag{7}$$

where [**I**] is the identity matrix and the stretch tensor [**U**] is symmetric:

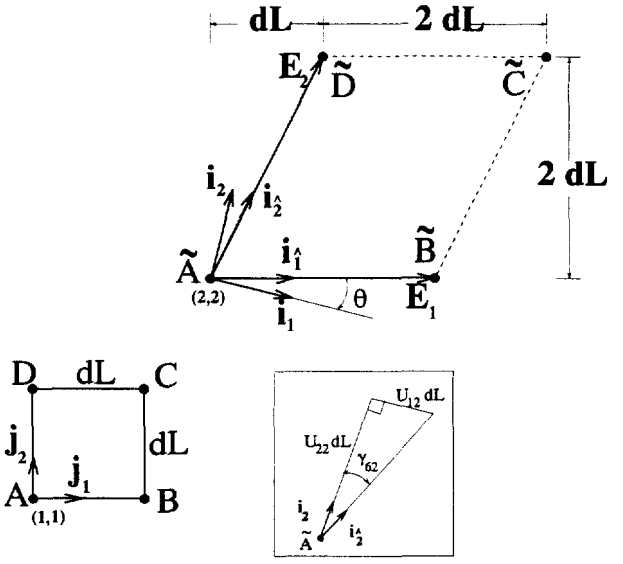

Fig. 2. Deformation of differential area *ABCD*.

$$[\mathbf{U}]^{\mathrm{T}} = [\mathbf{U}]. \tag{8}$$

The Green deformation tensor [C], is defined as (Malvern, 1969) $[\mathbf{F}]^{\mathrm{T}}[\mathbf{F}] = [\mathbf{U}]^2$. For any admissible (i.e., one-to-one) transformation between the x_i and the y_i, [C] is a positive definite symmetric matrix, and hence may be decomposed as (see, e.g., Strang 1988)

$$[\mathbf{C}] = [\mathbf{U}]^2 = [\mathbf{Q}][\Lambda][\mathbf{Q}]^{-1} \tag{9}$$

where [Q] is the matrix of eigenvectors of [C] and [Λ] is a diagonal matrix having the eigenvalues of [C] as its members. The matrix [U] may then be written as

$$[\mathbf{U}] = [\mathbf{Q}][\Lambda]^{-1/2}[\mathbf{Q}]^{-1}. \tag{10}$$

As a numerical example, consider the material point originally at $(x_1, x_2) = (1, 1)$ at time $t = 1$ s, with $a = 1\ \mathrm{m}^{-1}\ \mathrm{s}^{-1}$ and $b = 1\ \mathrm{s}^{-1}$. The deformation of an infinitesimal region near the point of interest is illustrated in Fig. 2. In the figure, the candidate point is A, and the undeformed region is described by the square $ABCD$. This square deforms to $\tilde{A}\tilde{B}\tilde{C}\tilde{D}$ through the relationships of eqns (3) and (4). Given the above parameters, the displacement gradient tensor [F] is given by

$$[\mathbf{F}] = \begin{bmatrix} 2 & 1 \\ 0 & 2 \end{bmatrix}, \tag{11}$$

whose eigenvalues Λ_i and eigenvectors $\mathbf{Q}_i$ are

$$\Lambda_1 = 2.43845, \quad \mathbf{Q}_1 = \begin{Bmatrix} -0.788205 \\ 0.625412 \end{Bmatrix} \quad \text{and} \quad \Lambda_2 = 6.56155, \quad \mathbf{Q}_2 = \begin{Bmatrix} -0.615412 \\ -0.788205 \end{Bmatrix}. \tag{12}$$

Hence [Λ] and [Q] are given by

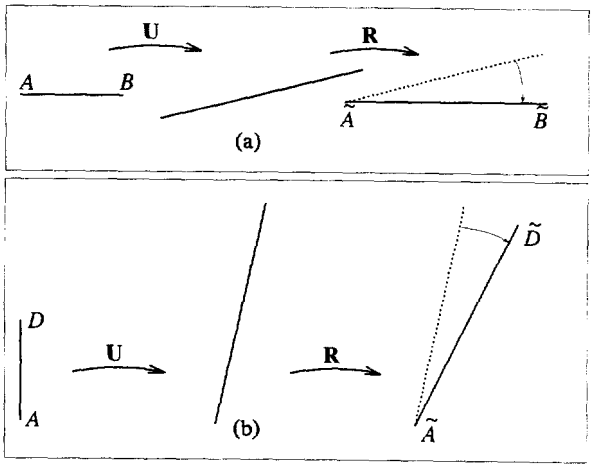

Fig. 3. Step-wise application of the polar decomposition method.

$$[\Lambda] = \begin{bmatrix} 2.43845 & 0 \\ 0 & 6.56155 \end{bmatrix}, \quad [\mathbf{Q}] = \begin{bmatrix} -0.788205 & -0.615412 \\ 0.615412 & -0.788205 \end{bmatrix}, \tag{13}$$

and from eqn (10) one obtains

$$[\mathbf{U}] = [\mathbf{Q}][\Lambda]^{-1/2}[\mathbf{Q}]^{-1} = \begin{bmatrix} 1.94029 & 0.485071 \\ 0.485071 & 2.18282 \end{bmatrix}, \tag{14}$$

and the rotation tensor is

$$[\mathbf{R}] = \begin{bmatrix} \cos\theta & \sin\theta \\ -\sin\theta & \cos\theta \end{bmatrix} = \begin{bmatrix} 0.970143 & 0.242536 \\ -0.242536 & 0.970143 \end{bmatrix}, \tag{15}$$

where $\theta = \cos^{-1} 0.970143 = 14.0362^\circ$ indicates the clockwise rotation of the **j**-frame to the **i**-frame. A more intuitive view of the polar decomposition may be seen by recognizing its application as

1. a stretch by the operator **U**
2. a rigid-body rotation by the operator **R**
3. and finally a translation to $\tilde{A}$.

Consider vector **AB** of Fig. 2 as these are applied (Fig. 3(a)). First, the stretch tensor of eqn (14) is applied to vector $\mathbf{AB} = \{dL, 0\}$:

$$\begin{bmatrix} 1.94029 & 0.485071 \\ 0.485071 & 2.18282 \end{bmatrix} \begin{Bmatrix} dL \\ 0 \end{Bmatrix} = \begin{Bmatrix} 1.94029\, dL \\ 0.485071\, dL \end{Bmatrix}, \tag{16}$$

Then this stretched fiber is rotated by [**R**] of eqn (15):

$$\begin{bmatrix} 0.970143 & 0.242536 \\ -0.242536 & 0.970143 \end{bmatrix} \begin{Bmatrix} 1.94029\, dL \\ 0.485071\, dL \end{Bmatrix} = \begin{Bmatrix} 2\, dL \\ 0 \end{Bmatrix}. \tag{17}$$

Likewise, applying the stretch tensor to vector $\mathbf{AD} = \{0, dL\}$ of Fig. 2 (see Fig. 3(b)) results in

$$\begin{bmatrix} 1.94029 & 0.485071 \\ 0.485071 & 2.18282 \end{bmatrix} \begin{Bmatrix} 0 \\ dL \end{Bmatrix} = \begin{Bmatrix} 0.485071\,dL \\ 2.18282\,dL \end{Bmatrix}. \tag{18}$$

Again, this stretched fiber is rotated by [**R**] of eqn (15):

$$\begin{bmatrix} 0.970143 & 0.242536 \\ -0.242536 & 0.970143 \end{bmatrix} \begin{Bmatrix} 0.485071\,dL \\ 2.18282\,dL \end{Bmatrix} = \begin{Bmatrix} dL \\ 2\,dL \end{Bmatrix}. \tag{19}$$

The Jaumann strain is given by

$$[\mathbf{B}] = [\mathbf{U}] - [\mathbf{I}] = \begin{bmatrix} 0.94029 & 0.485071 \\ 0.485071 & 1.18282 \end{bmatrix}. \tag{20}$$

(While not naming this strain "Jaumann" *per se*, Malvern (1969) refers to the components of [**B**] as "unit extensions" for direct strains referred to herein as B_{11} and B_{22} and "angle change" for the shear strain B_{12}. He notes that, in the finite deformation case, the so-called "angle change" is not the geometric angle change, but is dependent upon the stretches, as will be shown. He attributes his derivation to the works of Truesdell and Toupin (1960) and Eringen (1967).)

Note that eqn (20) includes only the elastic stretches at a material point (the rotation tensor is not present). In comparing this to eqn (1b), it is seen that the stretch tensor is equivalent to the gradient of the *local* displacement vector (given by **u** in eqn 1b) in the *rigidly rotated* coordinate system denoted by the $\{\mathbf{i}_{123}\}$-basis. The Green–Lagrange strain is given by (Malvern, 1969)

$$[\mathbf{L}] = \tfrac{1}{2}([\mathbf{U}]^2 - [\mathbf{I}]) = \begin{bmatrix} 1.5 & 1 \\ 1 & 2 \end{bmatrix}. \tag{21}$$

As an aside, while the tensors [**B**] and [**L**] above have different eigenvalues (principal strains), they have identical principal directions, as they should. The *values* of the principle strains are determined by the choice of measure (Jaumann vs Green), while the principle *directions* are not. Also note that the transformation between Green–Lagrange and Jaumann strains is given by (Pai and Palazotto, 1995b)

$$[\mathbf{L}] = \tfrac{1}{2}[\mathbf{B}]([\mathbf{U}] + [\mathbf{I}]), \tag{22}$$

and substituting the results into the above equation will verify the transformation.

A significant disparity between the two strain measures is seen, and the disparity is in both magnitude *and* direction. First consider the direct strains.

The Jaumann strain B_{22} has the direction illustrated in Fig. 2 by the unit vector $\mathbf{i}_2$, while the Green strain L_{22} is along $\mathbf{i}_2$. Now consider the strain magnitudes as they relate to the "fibers" forming the edges of the infinitesimal area $ABCD$. In particular, consider fiber AD which deforms to become $\tilde{A}\tilde{D}$. In deforming, the fiber has rotated $\arctan(dL/2\,dL) = 26.565^\circ$ clockwise, and has stretched to a new length of $[(2\,dL)^2 + dL^2]^{1/2} = \sqrt{5}\,dL$, a physical stretch of 123.6%. Clearly, neither the Jaumann strain, $B_{22} = 1.18282$ (from eqn (20)), nor the Green strain of $L_{22} = 2$ (from eqn (21)) are representing this physical stretch. The Green strain represents half the change in the squared length of the fiber, i.e., $\frac{1}{2}(\sqrt{5}^2 - 1^2) = 2$. The Jaumann strain $B_{22} = 1.18282$ represents the *projection* of the actual physical stretching of fiber AD onto the direction $\mathbf{i}_2$. This geometric meaning is shown as follows. Let the physical straining of fiber AD in the engineering strain sense be denoted by e_2 as:

$$e_2 = \frac{\|\tilde{A}\tilde{D}\| - \|AD\|}{\|AD\|} = \frac{\sqrt{5}\,dL - dL}{dL} = 1.23607. \tag{23}$$

Let the "stretch" of the fiber be defined as the ratio of the deformed length to the original length, or

$$U_{AD} = \|\tilde{A}\tilde{D}\|/\|AD\| = \sqrt{5}\,dx/dx = \sqrt{5} = 1+e_2 = 2.23607. \tag{24}$$

Now note the "shear" (rotation) angle associated with the '2' direction, denoted γ_{62} in Fig. 2. This angle may be used to find the projection of the stretch U_{AD} onto the $\mathbf{i}_2$ direction, U_{22} as

$$U_{22} = U_{AD}\cos\gamma_{62} = (1+e_2)\cos\gamma_{62} = 2.18282, \tag{25}$$

where γ_{62} is given by (the geometric interpretation of the angle may be seen in the inset of Fig. 2)

$$\gamma_{62} = \tan^{-1} U_{12}/U_{22}. \tag{26}$$

Note that the values of U_{12} and U_{22} of the right stretch tensor describe the stretching and rotation *due to deformation* of the infinitesimal fiber of length dL originally located along the $\mathbf{j}_2$ direction. Likewise, U_{11} and U_{12} describe the deformation of the fiber originally located along the $\mathbf{j}_1$ direction. Finally, the Jaumann strain, B_{22}, is seen to be

$$B_{22} = (1+e_2)\cos\gamma_{62} - 1 = 1.18282. \tag{27}$$

In the same manner, B_{11} describes the physical stretching of fiber AB projected onto the $\mathbf{i}_1$ direction. Notice that for small shear ($\cos\gamma_{62} \to 1$) the result yields the engineering strain result:

$$B_{22} = (1+e_2) - 1 = e_2 = 1.23607. \tag{28}$$

If the additional constraint of small direct strain is enforced, i.e., $e_2 \ll 1$ it is found that the Green strain approaches the engineering strain result as well. This may be shown as follows. The Green strain may be written as (note that $\mathbf{E}_2$ is the lattice vector related to the deformation of $dL\mathbf{j}_2$)

$$2L_{22} = \frac{\mathbf{E}_2\cdot\mathbf{E}_2 - dx^2}{dx^2} = \frac{(\sqrt{\mathbf{E}_2\cdot\mathbf{E}_2}+dx)(\sqrt{\mathbf{E}_2\cdot\mathbf{E}_2}-dx)}{dx^2}. \tag{29}$$

But for small strain, $\sqrt{\mathbf{E}_2\cdot\mathbf{E}_2} \approx dx$, leading to

$$2L_{22} \approx \frac{2\,dx(\sqrt{\mathbf{E}_2\cdot\mathbf{E}_2}-dx)}{dx^2} \approx 2\frac{(\sqrt{\mathbf{E}_2\cdot\mathbf{E}_2}-dx)}{dx} \approx 2e_2. \tag{30}$$

Examining the shear strains, from eqn (2b) it is seen that the shear strain L_{12} is simply the dot product of the lattice vectors.

$$L_{12} = \tfrac{1}{2}(\mathbf{E}_1\cdot\mathbf{E}_2) = 1. \tag{31}$$

In general, the lattice vectors are not of unit magnitude, so this strain is *not* the change in angle between two originally perpendicular fibers, which for this example is found from the geometry in Fig. 2 as

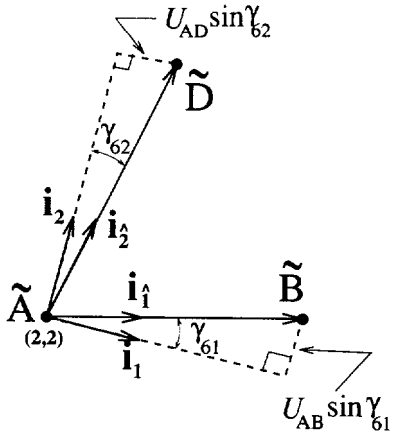

Fig. 4. Geometric interpretation of the Jaumann shear strain, B_{12}.

$$\tan\gamma_6 = \frac{dL}{2\,dL} = 0.5, \quad \text{or } \gamma_6 = 26.565^\circ = 0.46365 \text{ radians.} \tag{32}$$

From eqn (20) and the inset of Fig. 2, the Jaumann shear strain B_{12} is given by:

$$B_{12} = U_{12} = U_{22}\tan\gamma_{62} = 0.485071. \tag{33}$$

The first thing noticed is that $B_{12} = 0.485071$ radians is much closer to representing the actual angle change of $\gamma_6 = 0.46365$ radians than is $L_{12} = 1$. But why is it different at all? Consider Fig. 4 which describes the geometry of the problem. In terms of the geometry shown, the shear strain is given by

$$2B_{12} = U_{AB}\sin\gamma_{61} + U_{AD}\sin\gamma_{62} = (1+e_1)\sin\gamma_{61} + (1+e_2)\sin\gamma_{62}. \tag{34}$$

From this equation, it is seen that the tensorial strain, $2B_{12}$, approaches the physical angle change, γ_6, as both of the following are approached: (1) the stretch becomes negligible ($U_{AB} \to 1, U_{AD} \to 1$) and (2) the shearing angle is small ($\sin\gamma_{61} \to \gamma_{61}, \sin\gamma_{62} \to \gamma_{62}$). Under these conditions, the engineering strain result is obtained (see also Malvern, 1969)

$$2B_{12} = \gamma_6 = \gamma_{61} + \gamma_{62}. \tag{35}$$

To summarize, while both strain measures asymptotically approach the engineering strain values as strains become infinitesimal, the Jaumann measures are closely related to the engineering strains, even for small, but finite, strains. This is an important feature, as it allows constitutive data from experiments (engineering measures) to be used in the numerical analysis without transformation (a caveat is in order here: the lack of a need for transformation between stress measures reflects the use of the *nominal* or *engineering stress* which is referred to the undeformed cross-sectional area of the test specimen. This would reflect the use of test data at load levels below the ultimate load of the specimen, where necking of the specimen begins to occur. Beyond this load level, by assuming such plastic deformation occurs at constant volume, a corrected measure may be employed as shown by Malvern, 1969).

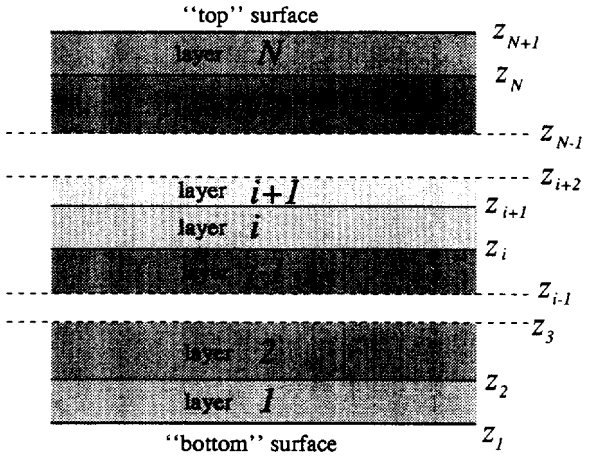

Fig. 5. A layered composite of N layers indicating ply numbering scheme and interface coordinates, z_i.

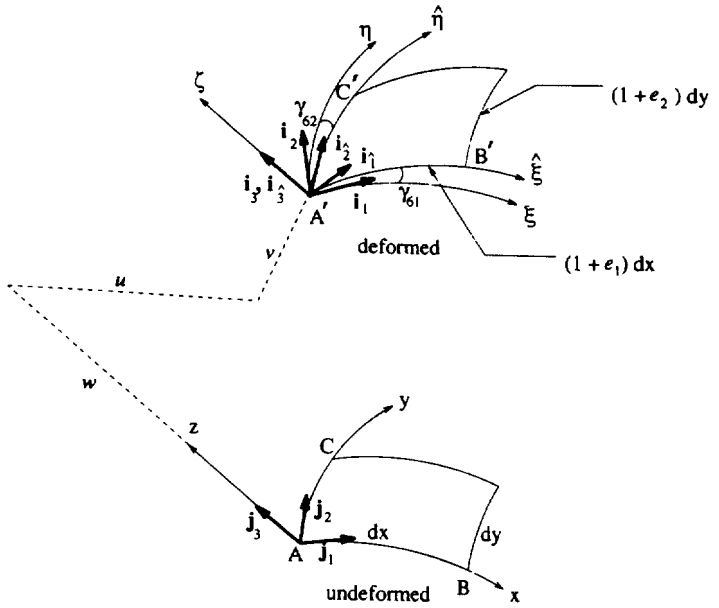

Fig. 6. Infinitesimal element undergoing deformation (after Pai and Palazotto, 1995a).

In a layered composite consisting of N layers (Fig. 5), the local displacement vector (with respect to the local $\xi\eta\zeta$ coordinate system of Fig. 6) as presented in Pai and Palazotto (1995a) and based upon the work of Bhimaraddi (1984), Reddy and Liu (1985), Kovařík (1980) is defined as (see Fig. 7)

$$\mathbf{u} = u_1^{(i)}\mathbf{i}_1 + u_2^{(i)}\mathbf{i}_2 + u_3^{(i)}\mathbf{i}_3 \tag{36}$$

where

$$\begin{aligned} u_1^{(i)} &= u_1^0(x,y) + z[\theta_2(x,y) - \theta_2^0(x,y)] + \gamma_5 z + \alpha_1^{(i)}(x,y)z^2 + \beta_1^{(i)}(x,y)z^3 \\ u_2^{(i)} &= u_2^0(x,y) - z[\theta_1(x,y) - \theta_1^0(x,y)] + \gamma_4 z + \alpha_2^{(i)}(x,y)z^2 + \beta_2^{(i)}(x,y)z^3 \\ u_3^{(i)} &= u_3^0(x,y) + \alpha_3^{(i)}(x,y)z + \beta_3^{(i)}(x,y)z^2. \end{aligned} \tag{37}$$

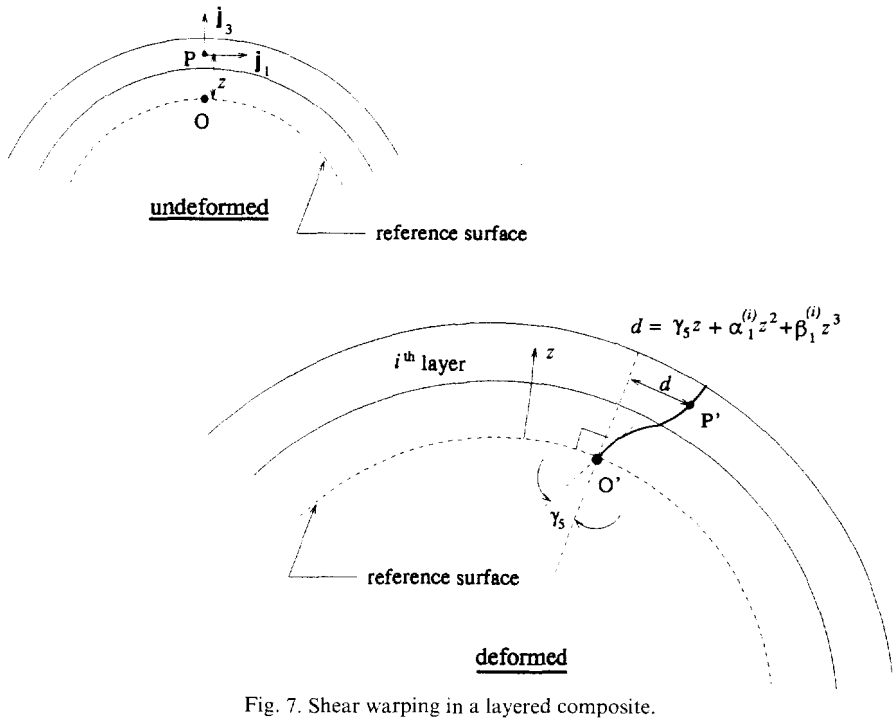

Fig. 7. Shear warping in a layered composite.

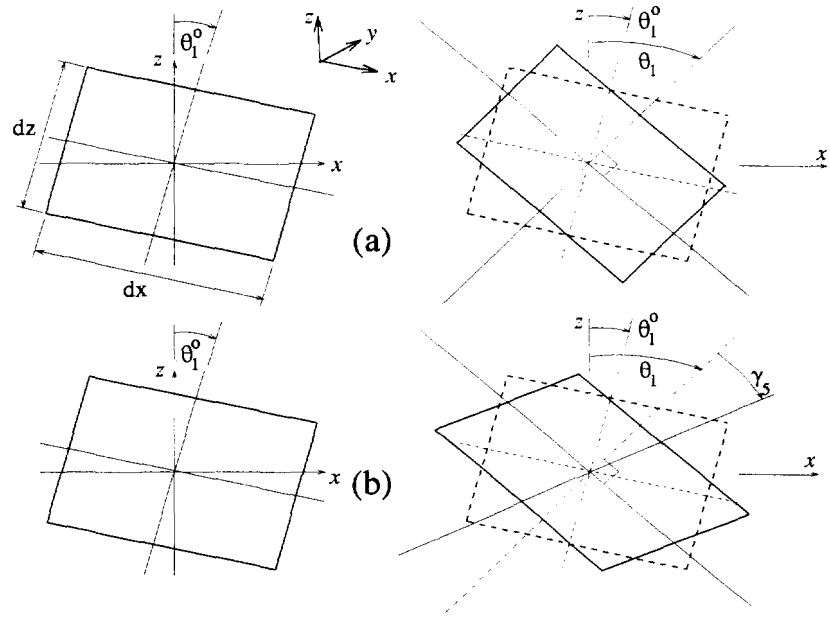

Fig. 8. Rigid rotations and shear rotations in an originally undeformed parallelogram; (a) rigid rotation without shear rotation; (b) rigid rotation with shear rotation.

Here, u_j^0 $(j = 1, 2, 3)$ are the components of displacement (with respect to the local coordinate system $\xi\eta\zeta$) of a point which is located on the reference surface at (x, y) before deformation. The rigid body rotations and shear rotations are given by θ and γ, respectively. In Fig. 8, these angles are graphically depicted in the xz plane. Referring to Fig. 8(a), the angle between the transverse coordinate (z) and the normal to the reference surface *in the undeformed configuration* as measured in the xz plane is given by θ_1^0. The corresponding angle in the yz plane (not shown) is given by $-\theta_2^0$ (the minus sign arises in employing the right-hand rule for rotation about the x-axis). The shear rotation angle in the xz plane at

the reference surface is denoted γ_5, and represents the rotation of the normal to the reference surface due to transverse shear deformation. The corresponding angle in the yz plane is γ_4 (the rotation direction for γ_4 is chosen such that a positive value of γ_4 gives positive displacement for points above the reference surface hence, unlike θ_2, its sign remains positive). At this point, having described the displacements u_j^0 and the rotations θ_j^0, θ_j, and γ_j, the ingredients are present for the so-called Reissner–Mindlin kinematic (see Reissner, 1945, 1947; Mindlin, 1951): normals to the reference surface may rotate due to shear, but must remain straight and of unchanged length. This assumption is inappropriate when dealing with laminated composites. A means is needed of including warping and stretching of the normal. For this the remaining terms of eqn (37) are used.

These terms, the $\alpha_k^{(i)}$ and $\beta_k^{(i)}$, are referred to as shear warping and thickness stretch functions. These functions are used to describe the kinematic behavior, *beyond simple rotation of the rigid normal*, of the material away from the reference surface, and allow coupling of the displacements $u_1^{(i)}$ and $u_2^{(i)}$ via the shear angles at the reference surface. That is, γ_4 can affect displacement $u_1^{(i)}$ through the warping functions and, likewise, γ_5 can affect $u_2^{(i)}$. By defining the shear warping functions, G_1 and G_2, and the thickness stretch function, G_3 as

$$G_1 \equiv \gamma_5 z + \alpha_1^{(i)} z^2 + \beta_1^{(i)} z^3, \quad G_2 \equiv \gamma_4 z + \alpha_2^{(i)} z^2 + \beta_2^{(i)} z^3, \quad \text{and} \quad G_3 \equiv \alpha_3^{(i)} z + \beta_3^{(i)} z^2, \tag{38}$$

the kinematics of eqn (37) may be written as

$$\begin{aligned} u_1^{(i)} &= u_1^0(x,y) + z[\theta_2(x,y) - \theta_2^0(x,y)] + G_1 \\ u_2^{(i)} &= u_2^0(x,y) - z[\theta_1(x,y) - \theta_1^0(x,y)] + G_2 \\ u_3^{(i)} &= u_3^0(x,y) + G_3. \end{aligned} \tag{39}$$

The coefficients of the shear warping functions are found by enforcing continuity of in-plane displacements and transverse shear stresses at the ply interfaces. This leads to a piece-wise continuous transverse shear stress field through the laminate thickness, as shown in Fig. 9. This figure depicts the transverse stresses in the 16-ply space shuttle nose-wheel tire

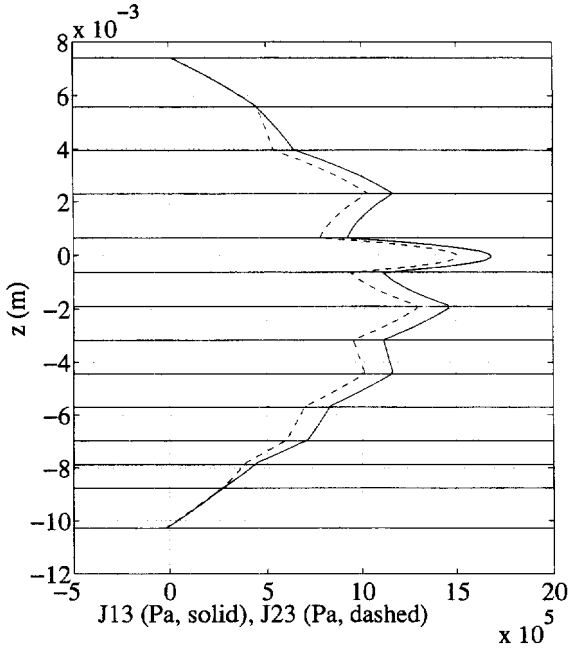

Fig. 9. Transverse shear stresses J_{13} and J_{23} through the thickness of the space shuttle nose wheel tire near the crown for a unit shear rotation at the reference surface ($z = 0$).

analyzed in subsequent sections. The magnitudes of the stresses are given per unit (1 rad) shear rotation at the reference surface.

Conspicuous by their absence in eqns (37) are the $(1 \pm z/R)$ terms associated with shell kinematics. These are the terms that account for the fact that, along a coordinate curve, normals separated by a finite distance are, in general, not parallel. The kinematics of eqn (37) neglect the "trapezoidal cross-section" effect, and hence are not "true" shell kinematics. The differential length subtended by a differential angle $d\theta$ changes with the thickness coordinate. This change in length is neglected in the analysis. While greatly simplifying the formulation, this does introduce an error. The error can be calculated as

$$\varepsilon = \frac{(R+\delta)\,d\theta - R\,d\theta}{R\,d\theta} = \delta/R, \tag{40}$$

where $\delta = \max\{|z_{N+1}|, |z_1|\}$ is the maximum distance of a fiber from the reference surface and R is the radius to the reference surface. Clearly, thick, deep shells will suffer the most error.

At this point, a simplification suggested by Pai and Palazotto (1995a) is performed: because G_3, the stretch in the thickness direction, is usually small, especially for thin shells, one may neglect G_3 and its derivatives in all strain–displacement expressions *except* in that of the direct normal strain, $B_{33}^{(i)}$. This is based upon the claim that the effect of transverse normal strain on the in-plane strains is negligible. Under this assumption, the strain–displacement relations become

$$B_{11}^{(i)} = \frac{\partial \mathbf{u}}{\partial x}\cdot \mathbf{i}_1 = (1+e_1)\cos\gamma_{61} - 1 + z(k_1 - k_1^0) + G_{1,x} - k_5 G_2 \tag{41a}$$

$$B_{22}^{(i)} = \frac{\partial \mathbf{u}}{\partial y}\cdot \mathbf{i}_2 = (1+e_2)\cos\gamma_{62} - 1 + z(k_2 - k_2^0) + G_{2,y} + k_4 G_1 \tag{41b}$$

$$B_{33}^{(i)} = \frac{\partial \mathbf{u}}{\partial z}\cdot \mathbf{i}_3 = G_{3,z} \tag{41c}$$

$$2B_{23}^{(i)} = \frac{\partial \mathbf{u}}{\partial y}\cdot \mathbf{i}_3 + \frac{\partial \mathbf{u}}{\partial z}\cdot \mathbf{i}_2 = G_{2,z} - k_{62} G_1 - k_2 G_2 \tag{41d}$$

$$2B_{13}^{(i)} = \frac{\partial \mathbf{u}}{\partial x}\cdot \mathbf{i}_3 + \frac{\partial \mathbf{u}}{\partial z}\cdot \mathbf{i}_1 = G_{1,z} - k_1 G_1 - k_{61} G_2 \tag{41e}$$

$$\begin{aligned} 2B_{12}^{(i)} &= \frac{\partial \mathbf{u}}{\partial x}\cdot \mathbf{i}_2 + \frac{\partial \mathbf{u}}{\partial y}\cdot \mathbf{i}_1 \\ &= (1+e_1)\sin\gamma_{61} + (1+e_2)\sin\gamma_{62} + z(k_6 - k_6^0) \\ &\quad + G_{1,y} + G_{2,x} + k_5 G_1 - k_4 G_2 \end{aligned} \tag{41f}$$

where, again, $k_6 \equiv k_{61} + k_{62}$ and $k_6^0 \equiv k_{61}^0 + k_{62}^0$.

To characterize a laminated composite made of transversely isotropic (sometimes called specially orthotropic or cross anisotropic) plys, well known tensor transformations are used (Whitney, 1987) to obtain the transformed stiffness matrix $[\bar{\mathbf{Q}}^{(i)}]$ for the ith lamina (see Fig. 5) from its principal stiffness matrix $[\mathbf{Q}^{(i)}]$ and its ply angle, which is measured with respect to the x axis. Note that in this theoretical development, changes in the relative fiber orientations from ply-to-ply due to deformation are neglected. That is, under the assumption of a perfect interply bond, the deformation cannot cause the relative angle between fibers in, for example, the ith ply, to *change* their orientation relative to the fibers of the $i-1$st or $i+1$st plies. In actuality, such orientation changes do take place, as

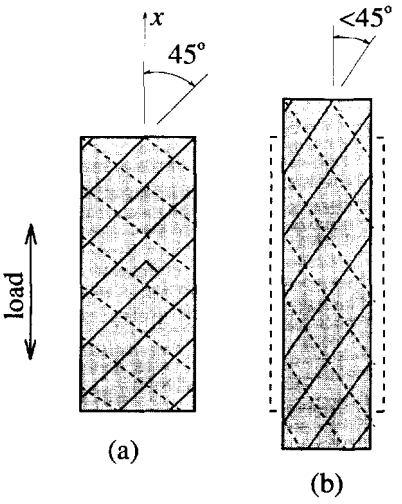

Fig. 10. Change in orientation of fibers during deformation; (a) angle-ply laminate before deformation, (b) after deformation.

illustrated in Fig. 10. In the figure, a two-ply laminated composite is depicted. The "top" ply has fibers originally oriented 45° to the x-axis, while the "bottom" ply has fibers oriented at $-45°$ (the fibers of this ply are depicted as dashed lines). During deformation, a "scissoring" of the fibers takes place due to the stretching of the material in the x-direction. In the current formulation, such changes in orientation are not accounted for. To account for such deformation would require tracing the in-plane deformation at each location (in x, y, and z), and recalculating the constitutive relations based on any changes in the orientations. In large strain analyses using a Green's strain total-Lagrangian approach, such as that of Schimmels and Palazotto (1994), expensive transformations of material and constitutive frames-of-reference are used to follow global changes of fiber orientations.

A transversely isotropic material can be described in terms of five independent elastic constants:

$$E_{11}, \quad E_{22} = E_{33}, \quad G_{23} \text{ or } \nu_{23}, \quad G_{12} = G_{13}, \quad \nu_{12} = \nu_{13}. \tag{42}$$

The quantities G_{23} and ν_{23} are related by (Whitney, 1987):

$$G_{23} = \frac{E_{23}}{2(1+\nu_{23})}, \tag{43}$$

so either, but not both, may be specified.

The relationship between the Jaumann stresses, J_{mn}, and the Jaumann (or Biot–Cauchy Jaumann) strains, B_{mn}, for the ith lamina of a transversely isotropic material may then be written as (for the transformed relationships)

$$\begin{Bmatrix} J_{11}^{(i)} \\ J_{22}^{(i)} \\ J_{33}^{(i)} \\ J_{12}^{(i)} \\ J_{23}^{(i)} \\ J_{13}^{(i)} \end{Bmatrix} = \begin{bmatrix} \bar{Q}_{11}^{(i)} & \bar{Q}_{12}^{(i)} & \bar{Q}_{13}^{(i)} & \bar{Q}_{16}^{(i)} & 0 & 0 \\ \bar{Q}_{12}^{(i)} & \bar{Q}_{22}^{(i)} & \bar{Q}_{23}^{(i)} & \bar{Q}_{26}^{(i)} & 0 & 0 \\ \bar{Q}_{13}^{(i)} & \bar{Q}_{23}^{(i)} & \bar{Q}_{33}^{(i)} & \bar{Q}_{36}^{(i)} & 0 & 0 \\ \bar{Q}_{16}^{(i)} & \bar{Q}_{26}^{(i)} & \bar{Q}_{36}^{(i)} & \bar{Q}_{66}^{(i)} & 0 & 0 \\ 0 & 0 & 0 & 0 & \bar{Q}_{44}^{(i)} & \bar{Q}_{45}^{(i)} \\ 0 & 0 & 0 & 0 & \bar{Q}_{45}^{(i)} & \bar{Q}_{55}^{(i)} \end{bmatrix} \begin{Bmatrix} B_{11}^{(i)} \\ B_{22}^{(i)} \\ B_{33}^{(i)} \\ 2B_{12}^{(i)} \\ 2B_{23}^{(i)} \\ 2B_{13}^{(i)} \end{Bmatrix} \tag{44}$$

The principle of virtual work, which will be used in the finite element development, states (Washizu, 1982)

$$\int_0^T (-\delta\Pi + \delta W_{nc})\,\mathrm{d}t = 0 \tag{45}$$

where Π and W_{nc} denote the elastic energy and the non-conservative energy due to applied loads (by letting W consist of both conservative and non-conservative forces, eqn (45) is sometimes referred to as the *extended Hamilton principle* (Meirovitch, 1967)). The non-conservative energy includes the energy due to surface loads (distributed or concentrated).

The Jaumann stresses and strains are *work conjugate*, that is, the elastic energy, Π, of the structure may be entirely accounted for by integrating the product of the stresses and strains over the entire volume of the structure:

$$\Pi = \frac{1}{2}\sum_{i=1}^{N}\int\int\int_V [\mathbf{J}^{(i)}]^{\mathrm{T}}[\mathbf{B}^{(i)}]\,\mathrm{d}V. \tag{46}$$

Or, since $[\mathbf{J}^{(i)}] = [\bar{\mathbf{Q}}^{(i)}][\mathbf{B}^{(i)}]$ and $[\bar{\mathbf{Q}}^{(i)}]$ is symmetric,

$$\Pi = \frac{1}{2}\sum_{i=1}^{N}\int\int\int_V [\mathbf{B}^{(i)}]^{\mathrm{T}}[\bar{\mathbf{Q}}^{(i)}][\mathbf{B}^{(i)}]\,\mathrm{d}V. \tag{47}$$

The first variation of the potential energy is then found through

$$\begin{aligned}\delta\Pi &= \frac{1}{2}\sum_{i=1}^{N}\int\int\int_V \delta[\mathbf{B}^{(i)}]^{\mathrm{T}}[\bar{\mathbf{Q}}^{(i)}][\mathbf{B}^{(i)}] + [\mathbf{B}^{(i)}]^{\mathrm{T}}[\bar{\mathbf{Q}}^{(i)}]\,\delta[\mathbf{B}^{(i)}]\,\mathrm{d}V \\ &= \sum_{i=1}^{N}\int\int\int_V \delta[\mathbf{B}^{(i)}]^{\mathrm{T}}[\bar{\mathbf{Q}}^{(i)}][\mathbf{B}^{(i)}]\,\mathrm{d}V,\end{aligned} \tag{48}$$

where V is the undeformed volume of the shell structure and (i) refers to the value of the function in the ith layer of the laminate.

To this point, the displacement field has not been approximated, so the expressions for the elastic energy and its variation could be considered "exact". But in order to numerically solve the equations, the displacements must be approximated. This is done by assuming that the displacement field may be represented by polynomial functions (shape functions) over some finite region (the finite element). Moreover, it is assumed that if the domain is made up of a sufficient number of such elements, the solution will provide acceptable results.

Toward this end, the components of $\{\mathbf{U}\}$ are approximated through the choice of a specific finite element. Using shape functions to discretize the displacements, one obtains

$$\{u, v, w, \gamma_4, \gamma_5\}^{\mathrm{T}} = [\mathbf{N}(r, s)]\{\mathbf{q}^{[j]}\}, \tag{49}$$

where $\{\mathbf{q}^{[j]}\}$ is the vector whose members are the nodal displacements of element j, and $[\mathbf{N}(r, s)]$ is a matrix of two-dimensional finite element shape functions written in terms of natural coordinates r and s, and given by

$$[\mathbf{N}] \equiv \begin{bmatrix} \mathscr{H}_1^1 & 0 & 0 & 0 & 0 \\ \mathscr{H}_2^1 & 0 & 0 & 0 & 0 \\ \mathscr{H}_3^1 & 0 & 0 & 0 & 0 \\ 0 & \mathscr{H}_1^1 & 0 & 0 & 0 \\ 0 & \mathscr{H}_2^1 & 0 & 0 & 0 \\ 0 & \mathscr{H}_3^1 & 0 & 0 & 0 \\ 0 & 0 & \mathscr{H}_1^1 & 0 & 0 \\ 0 & 0 & \mathscr{H}_2^1 & 0 & 0 \\ 0 & 0 & \mathscr{H}_3^1 & 0 & 0 \\ 0 & 0 & 0 & \mathscr{L}_1 & 0 \\ 0 & 0 & 0 & 0 & \mathscr{L}_1 \\ \mathscr{H}_1^2 & 0 & 0 & 0 & 0 \\ \mathscr{H}_2^2 & 0 & 0 & 0 & 0 \\ \mathscr{H}_3^2 & 0 & 0 & 0 & 0 \\ 0 & \mathscr{H}_1^2 & 0 & 0 & 0 \\ 0 & \mathscr{H}_2^2 & 0 & 0 & 0 \\ 0 & \mathscr{H}_3^2 & 0 & 0 & 0 \\ 0 & 0 & \mathscr{H}_1^2 & 0 & 0 \\ 0 & 0 & \mathscr{H}_2^2 & 0 & 0 \\ 0 & 0 & \mathscr{H}_3^2 & 0 & 0 \\ 0 & 0 & 0 & \mathscr{L}_2 & 0 \\ 0 & 0 & 0 & 0 & \mathscr{L}_2 \\ \mathscr{H}_1^3 & 0 & 0 & 0 & 0 \\ \mathscr{H}_2^3 & 0 & 0 & 0 & 0 \\ \mathscr{H}_3^3 & 0 & 0 & 0 & 0 \\ 0 & \mathscr{H}_1^3 & 0 & 0 & 0 \\ 0 & \mathscr{H}_2^3 & 0 & 0 & 0 \\ 0 & \mathscr{H}_3^3 & 0 & 0 & 0 \\ 0 & 0 & \mathscr{H}_1^3 & 0 & 0 \\ 0 & 0 & \mathscr{H}_2^3 & 0 & 0 \\ 0 & 0 & \mathscr{H}_3^3 & 0 & 0 \\ 0 & 0 & 0 & \mathscr{L}_3 & 0 \\ 0 & 0 & 0 & 0 & \mathscr{L}_3 \\ \mathscr{H}_1^4 & 0 & 0 & 0 & 0 \\ \mathscr{H}_2^4 & 0 & 0 & 0 & 0 \\ \mathscr{H}_3^4 & 0 & 0 & 0 & 0 \\ 0 & \mathscr{H}_1^4 & 0 & 0 & 0 \\ 0 & \mathscr{H}_2^4 & 0 & 0 & 0 \\ 0 & \mathscr{H}_3^4 & 0 & 0 & 0 \\ 0 & 0 & \mathscr{H}_1^4 & 0 & 0 \\ 0 & 0 & \mathscr{H}_2^4 & 0 & 0 \\ 0 & 0 & \mathscr{H}_3^4 & 0 & 0 \\ 0 & 0 & 0 & \mathscr{L}_4 & 0 \\ 0 & 0 & 0 & 0 & \mathscr{L}_4 \end{bmatrix}^{\mathbf{T}} . \tag{50}$$

The shape functions are given by

$$\mathscr{H}_1^k = 1/8(1+r_k r)(1+s_k s)(2+r_k r+s_k s-r^2-s^2) \tag{51a}$$

$$\mathscr{H}_2^k = (a/8)r_k(1+r_k r)^2(r_k r-1)(1+s_k s) \tag{51b}$$

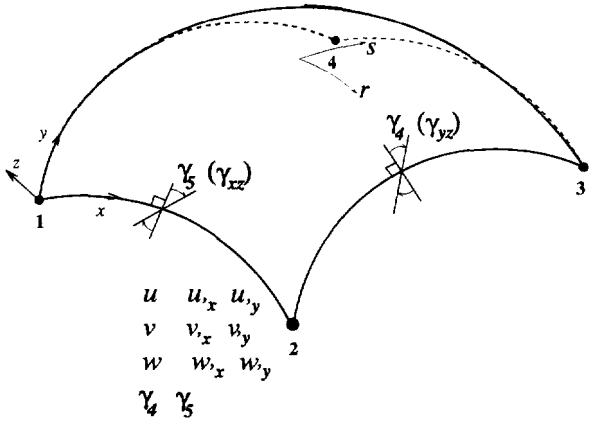

Fig. 11. The 44-DOF shell element.

$$\mathscr{H}_3^k = (b/8)s_k(1+r_k r)(s_k s-1)(1+s_k s)^2 \tag{51c}$$

$$\mathscr{L}^k = (1/4)(1+r_k r)(1+s_k s) \tag{51d}$$

where $2a$ and $2b$ are dimensions along x and y of the rectangular (in curvilinear coordinates) element, and the values of r_k and s_k are determined by the local coordinates (r, s) of the kth node.

Again, u, v, and w are displacements relative to the undeformed local curvilinear system, and γ_4 and γ_5 represent reference surface shear rotation angles in the η–ζ and ξ–ζ planes, respectively, expressed in terms of the global coordinates.

For the present research, a 4-noded, 44 DOF finite element is employed.

Figure 11 shows the four-noded 44 DOF element. The degrees of freedom at each corner are u, $u_{,x}$, $u_{,y}$, v, $v_{,x}$, $v_{,y}$, w, $w_{,x}$, $w_{,y}$, γ_4, and γ_5. Hermitian shape functions are used for all DOF except the transverse shear DOF, γ_4 and γ_5, which use bi-linear shape functions.

Employing this finite element leads to equations having the following form. The formulation of the matrices in these equations is described in detail in the references of Pai and Palazotto (1995a) and Greer (1996).

$$\underset{44\times 44}{[\check{\mathbf{K}}^{[j]}]} = \int\int_{A^{[j]}} \underset{44\times 24}{[\mathbf{D}]^{\mathrm{T}}} \left(\underset{24\times 12}{[\boldsymbol{\Psi}^0]^{\mathrm{T}}} \underset{12\times 12}{[\boldsymbol{\Phi}]} \underset{12\times 24}{[\boldsymbol{\Psi}^0]} + \underset{24\times 24}{[\boldsymbol{\Upsilon}]}\right) \underset{24\times 44}{[\mathbf{D}]}\, \mathrm{d}x\,\mathrm{d}y \tag{52}$$

and

$$\underbrace{[\mathbf{K}^{[j]}]\{\mathbf{q}^{[j]}\}}_{44\times 1}\Big|_{\{\mathbf{q}^{[j]}\}=\{\mathbf{q}^0\}} = \int\int_{A^{[j]}} \underset{44\times 1}{[\mathbf{D}]^{\mathrm{T}}} \underset{24\times 12}{[\boldsymbol{\Psi}^0]^{\mathrm{T}}} \underset{12\times 12}{[\boldsymbol{\Phi}]} \underset{12\times 1}{\{\psi^0\}}\, \mathrm{d}x\,\mathrm{d}y, \tag{53}$$

where $[\mathbf{K}^{[j]}]$ is the so-called tangent stiffness matrix, and $[\mathbf{K}^{[j]}]\{\mathbf{q}^{[j]}\}$ represents the product of the (also displacement dependent) stiffness matrix and the current nodal displacements. Note that the $[\mathbf{K}^{[j]}]$ of eqn (52) is a symmetric matrix. Furthermore, note that eqn (53) describes the resultant force vector

$$\{\mathbf{R}^{[j]}\} = [\mathbf{K}^{[j]}]\{\mathbf{q}^{[j]}\}\,|_{\{\mathbf{q}^{[j]}\}=\{\mathbf{q}^0\}}. \tag{54}$$

This will be useful for calculations of nodal loads in subsequent sections.

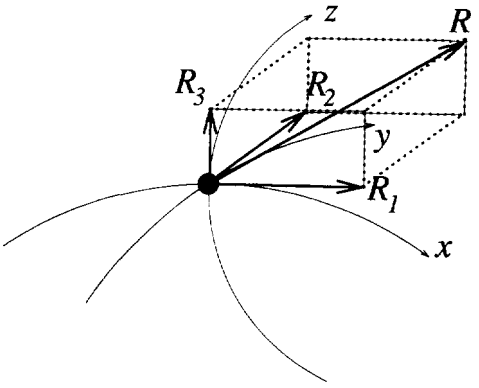

Fig. 12. Load **R** acting at a node and its components along the Lagrangian coordinate axes.

3. EXTERNAL LOADS

Using eqn (49) the variation of non-conservative energy due to external loads is

$$\begin{aligned}\delta W_{nc} &= \iint \{\delta u, \delta v, \delta w, \delta\gamma_4, \delta\gamma_5\}\{R_1, R_2, R_3, 0, 0\}^{\mathrm{T}}\,\mathrm{d}x\,\mathrm{d}y \\ &= \sum_{j=1}^{N_e}\iint_{A^{[j]}}\{\delta\mathbf{q}^{[j]}\}^{\mathrm{T}}[\mathbf{N}]^{\mathrm{T}}\{R_1, R_2, R_3, 0, 0\}^{\mathrm{T}}\,\mathrm{d}x\,\mathrm{d}y \\ &= \sum_{j=1}^{N_e}\{\delta\mathbf{q}^{[j]}\}^{\mathrm{T}}\{\mathbf{R}^{[j]}\} \\ &= \{\delta\mathbf{q}\}^{\mathrm{T}}\{\mathbf{R}\} \end{aligned} \tag{55}$$

where R_1, R_2, and R_3 are distributed external loads along the directions of the axes x, y, and z, respectively (see Fig. 12). Normal and tangential loads on the shell are most easily described in terms of these shell curvilinear coordinates. The global structural loading vector is $\{\mathbf{R}\}$, and $\{\mathbf{R}^{[j]}\}$ is the elemental nodal loading vector, which is given by

$$\underset{44\times 1}{\{\mathbf{R}^{[j]}\}} \equiv \iint_{A^{[j]}}[\mathbf{N}]^{\mathrm{T}}\{R_1, R_2, R_3, 0, 0\}^{\mathrm{T}}\,\mathrm{d}x\,\mathrm{d}y. \tag{56}$$

Here, it is assumed that R_1, R_2, and R_3 are functions of x and y only and not functions of displacements u, v, w. Some loading scenarios, such as tire pressurization, may need to be described in terms of the deformed surface. This is easily handled by applying the load incrementally.

4. SOLUTION TO INCREMENTAL EQUATIONS

As incremental/iterative Newton–Raphson method is used to solve the nonlinear finite element equations:

$$\sum_{j=1}^{N_e}[\check{\mathbf{K}}^{[j]}]\{\Delta\mathbf{q}^{[j]}\} = \sum_{j=1}^{N_e}(\{\mathbf{R}^{[j]}\} - [\mathbf{K}^{[j]}]\{\mathbf{q}^{[j]}\})_{\{\mathbf{q}^{[j]}\}=\{\mathbf{q}^0\}}. \tag{57}$$

Again, the asymmetric stiffness matrix $[\mathbf{K}^{[j]}]$ need never be formulated, since the product $[\mathbf{K}^{[j]}]\{\mathbf{q}^{[j]}\}$ is a vector described by eqn (53). Hence, in the implementation of the algorithm, routines for manipulating and storing real symmetric matrices may be employed.

In nonlinear analyses, the solution to eqn (57) is found through an iterative process. In this iterative process, some sort of criterion must be used to determine when the "correct" solution to the finite element equations has been found. In the finite element literature, such

criteria are referred as *convergence* (Owen and Hinton 1980) or, more correctly *termination* criteria (Cook *et al.* 1989). (The word *convergence* implies certain strict mathematical properties not satisfied by termination criteria. Furthermore, *convergence* in the finite element sense is more properly applied to characteristics of particular finite elements to provide convergent solutions—a topic of an enormous body of literature that *does* involve convergence in the mathematically rigorous sense.)

The criterion used in the current work (Owen and Hinton, 1980; Palazotto and Dennis, 1992) compares successive displacement solution vectors to quantitatively assess the "correctness" of the solution. The global displacement solution vector $\{\mathbf{q}\}$ for the $i+1$st iteration is compared to that of the ith iteration in the current displacement increment as follows:

$$\left| \frac{\|\{\mathbf{q}\}\|_{i+1} - \|\{\mathbf{q}\}\|_i}{\|\{\mathbf{q}\}\|_1} \right| \times 100 \leqslant \varepsilon, \tag{58}$$

where $\|\{\mathbf{q}\}\|$ is the Euclidean norm of the displacement vector $\{\mathbf{q}\}$ having n elements such that

$$\|\{\mathbf{q}\}\| = \sqrt{\sum_{i=1}^{n} (q_i)^2}. \tag{59}$$

5. THE COMPUTER PROGRAM

The program used for the current analysis is written in FORTRAN. The length of the code is approximately 50,000 lines, with the vast majority of the code devoted to developing the transformation matrix [**T**] and the deformed curvatures k_i needed to update the stiffness matrices at each iteration of each displacement increment. Much of the code was generated with the help of *Mathematica*, the symbolic mathematics software of Wolfram Research, Inc. The need for using the software became apparent in attempting to form the expressions for the derivatives required to generate the $[\mathbf{\Psi}^0]$ and $[\Upsilon]$ matrices of eqn (52).

The code has been used to analyze isotropic and laminated flat plates and beams, cylindrical shells and arches, circular toroidal shells and toroidal shells of very general cross-section. Analyses for shells of multiple curvature (like the toroidal shell) are more computationally intensive, as the undeformed curvatures change when moving along a coordinate curve. These curvatures must be calculated at each Gauss point during the stiffness matrix integration process for each iteration of each displacement increment. In all analyses, including flat plates, the deformed curvatures must be calculated at each Gauss point in order to generate the new warping/stretching functions at that point and the attendant constitutive array, [**Φ**].

For these analyses, the program was run on the SparcStation 20 workstation. Typical run times were of the order of five minutes to several hours depending on the application.

6. APPLICATION TO THE AIRCRAFT TIRE

There is a large body of excellent work in the analysis of tires through the use of the finite element method. Nonetheless, the present research is novel in its combining of a number of heretofore disparate features: (1) a high-fidelity geometric model of the anisotropic tire is developed entirely with two-dimensional finite elements. (2) This model incorporates a higher order and layer-wise shear deformation shell theory and includes thickness stretching. (3) The model includes the effects of large displacements and rotations (i.e., geometric nonlinearity).

By way of comparison, the work of Kim and Noor (1990) incorporated a geometrically high-fidelity tire model, but not higher order shear nor thickness stretching. Many simplified models, such as the ring on an elastic foundation or simple shells of revolution (Padovan,

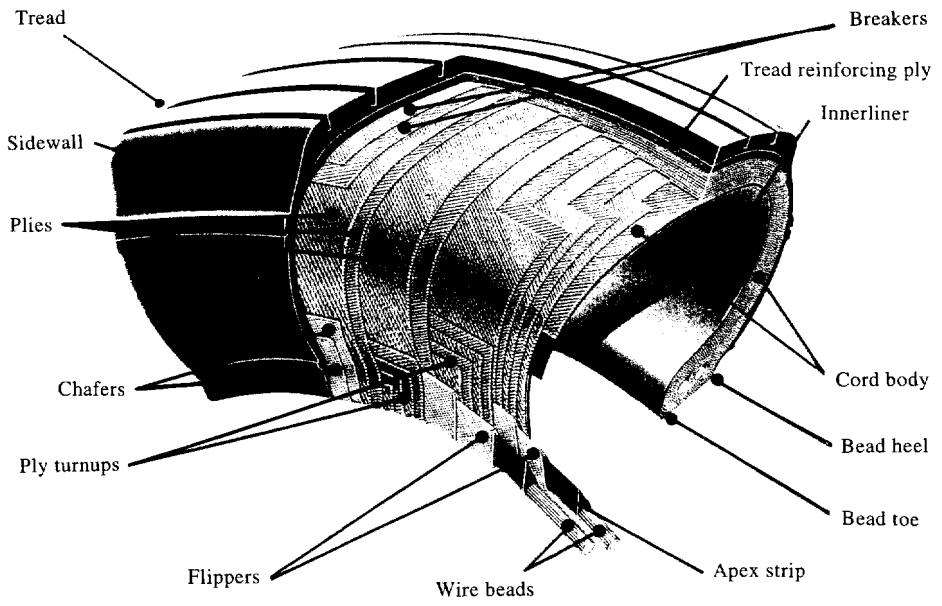

Fig. 13. Typical bias-ply aircraft tire indicating complexity of construction.

1975, 1976, 1977; Kennedy and Padovan, 1987; Brockman *et al.*, 1992) have been used for analytical and finite element dynamic analyses, usually employing the Galilean transform (Sve and Herrmann, 1974) in concert with traveling load methods. Others have used three-dimensional finite elements (Kennedy and Padovan, 1987; Brockman *et al.*, 1992; Wu and Du, 1995) having, to varying degrees, simplified material models. Such simplifications often take the form of generating single-ply models having "equivalent orthotropic" properties or just including fewer plies in the model than exist in the actual tire. Others simplify the finite element itself, as did DeEskinazi *et al.* (1978), who used flat triangular plate elements to model the radial tire. Incorporation of the viscoelastic properties of rubber, not included herein, has also been done using the finite element method (see, e.g., Padovan (1976), Kennedy and Padovan (1987)).

The aircraft tire (Fig. 13) is a toroidal shell of non-circular cross-section. Furthermore, it may be described as a laminated shell, owing to its corded-rubber ply construction. The structure is complicated by the presence of bead rings and tread grooves, as well as by the varying thickness of the cross-section in the meridional direction (throughout this discussion, "circumferential" refers to the x, or "rolling" direction, while "meridional" refers to the y, or "minor radius" direction). The thickness, number of plys, ply orientation, and constitutive properties all change in the meridional direction.

The two types of mechanical loads on the tire are inflation loads and loads caused by contact with a surface. Inflation forces are easily described by the "tire pressure", while the loads due to contact depend on many factors, including aircraft weight, braking, pavement roughness and flexibility, tire camber, turning loads, etc. The effect of inflation on the tire is examined herein.

For the finite element model, the generatrix (tire cross-section) for the shell of revolution is represented by a tension spline (Renka, 1987) connecting user-defined nodes along the cross section. Rotating this generatrix about the origin of the major radius (axle) of the shell then generates the tire's reference surface. The tension spline is used because, in addition to having the continuous second derivative of the classical cubic spline (which results in continuous curvature), it may be formulated to preserve convexity of the curve over an interval. That is, the tension may be chosen such that the interpolant may not "wiggle" (have an inflection point) between data points. This results in a smooth generatrix, making it suitable for modeling the tire cross section (Kim and Noor, 1990). Renka's technique uses an iterative procedure to satisfy certain user-defined conditions on the interpolant with the minimum tension, σ, necessary. The interested reader is referred to the reference of Renka (1987) for the details of the algorithm.

The FORTRAN implementation of this technique downloaded from the world-wide-web site

$$\text{http://netlib.att.com/netlib/master/readme.html} \tag{60}$$

provides for calculation of the derivatives of the fitted curve at any point along the curve.

7. THE SHUTTLE TIRE

The nose wheel tire of the Space Transportation System or "Space Shuttle" is examined in the current research. The tire is modeled as a two-dimensional reference surface, and the ply thicknesses, ply constitutive relations, and ply orientation angles are allowed to change from element to element in the meridional direction (elements in the circumferential direction have identical properties). The tire's construction details are described in the work of Kim and Noor (1990) whose results are used for comparison purposes in the current research.

7.1. *Inflation*

In the current work, a pressure loading is applied using equivalent nodal loads. The shape functions are used to calculate the applied nodal loads in a potential energy equivalent sense. That is,

$$\underset{44\times 1}{\{\mathbf{r}_e\}} = \int_A \underset{44\times 5}{[\mathbf{N}]^{\mathrm{T}}} \underset{5\times 1}{\{\mathbf{P}\}}\, \mathrm{d}A \tag{61}$$

where $\{\mathbf{r}_e\}$ is the vector of equivalent nodal loads for the element, [N] is the matrix of shape functions (eqn 51), and

$$\{\mathbf{P}\} = \{0, 0, p_w, 0, 0\} \tag{62}$$

is the pressure loading vector.

The results of the finite element analysis for an inflation pressure of 2.206 MPa (320 psi) are compared to experimental results presented by Kim and Noor (1990) using the mesh of Fig. 14. The reference surface is chosen to satisfy three criteria: (1) along the meridian, the reference surface should be as near the middle of the laminate as possible, (2) the reference surface should be at the middle of the ply in which it resides, and (3) the outer

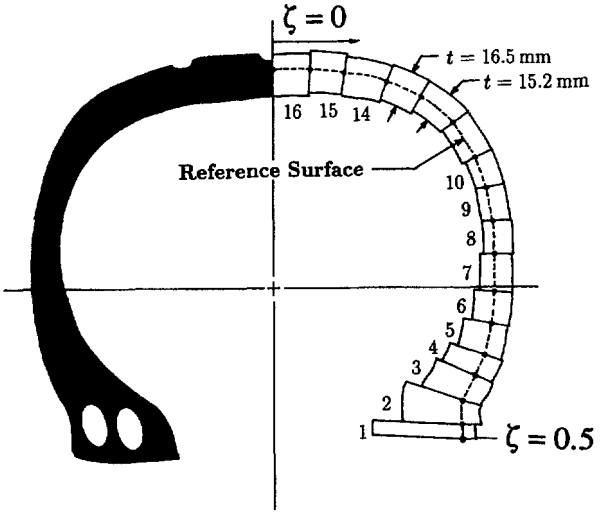

Fig. 14. Finite element mesh vs. actual tire cross-section indicating element numbering and typical element thicknesses.

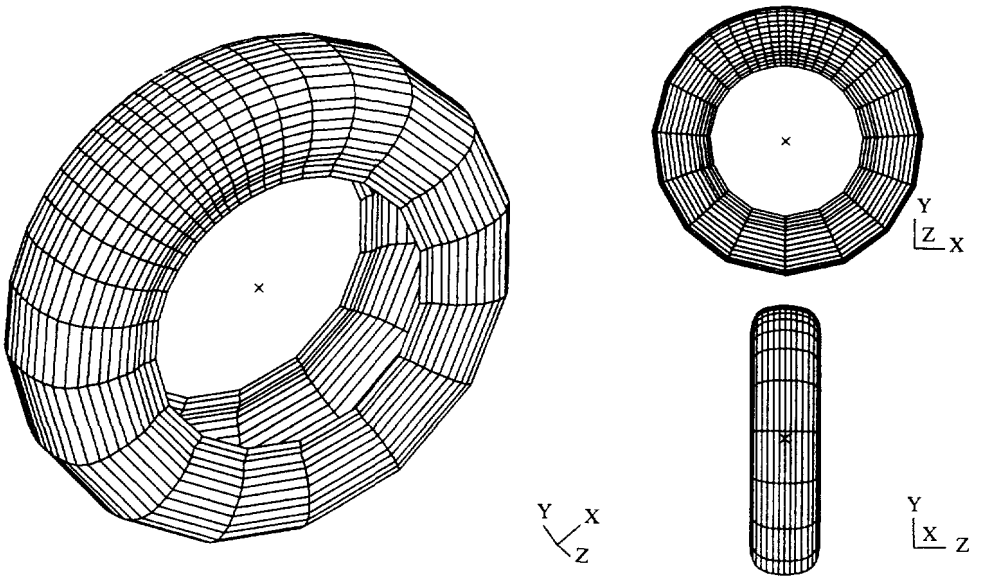

Fig. 15. Three views of the shuttle nose wheel tire mesh; the figure does not reflect the fact that the finite element is actually bi-curved, not flat.

surface of the elements should match that of the actual tire and be as smooth as possible. Criterion (1) arises from the desire to free the warping functions in the outer plys; the ply containing the reference surface must be constrained such that the warping functions are zero at the reference surface. Criterion (2) reflects that fact that as the reference surface approaches a ply interface, the warping function equations have no unique solution, hence the middle of the ply is a desirable location (Pai, 1995). The third criterion is desirable from the standpoint of tire contact studies as, in reality, the outer surface is the contact surface. In the contact algorithm, the reference surface is used as the contact surface, then corrected for the thickness of the tire above the reference surface as well as the change in that thickness. Since the reference surface is continuous and smooth, criterion (3) ensures that the undeformed tire thickness above the reference surface is nearly uniform about the meridian.

Trying to satisfy these criteria leads to the element choices depicted in Fig. 14, where ζ is the non-dimensionalized meridional coordinate, expressing the fraction of the total curvilinear length along the meridian of the reference surface. The overall mesh employed in the inflation study is shown in Fig. 15, where refinement in one area of the mesh anticipates future work studies of tire contact in that region. The mesh employs 832 elements, 858 nodes, and has 9438 total DOF. The material properties used in the finite element model are presented in the Appendix. The boundary conditions for the analysis are given by

$$\begin{aligned}
&\text{at } y = 0, \quad \text{clamped: all DOF fixed}\\
&\text{at } y = 9.13\,\text{mm}, \quad \text{clamped: all DOF fixed}\\
&\text{at } y = 16.60\,\text{mm}, \quad \text{clamped: all DOF fixed}\\
&\text{at } y = 439.29\,\text{mm}, \quad \text{clamped: all DOF fixed}\\
&\text{at } y = 446.75\,\text{mm}, \quad \text{clamped: all DOF fixed}\\
&\text{at } y = 455.88\,\text{mm}, \quad \text{clamped: all DOF fixed.}
\end{aligned} \tag{63}$$

These conditions reflect the fact that the first and last three (circumferential) rows of nodes

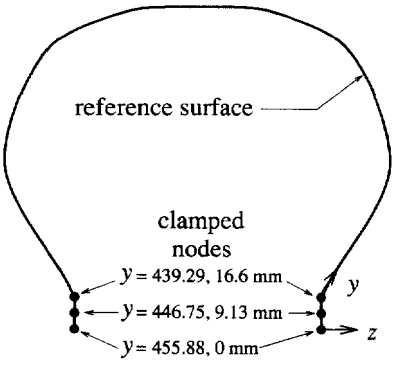

Fig. 16. Tire cross section (not to scale) indicating coordinate system and boundary conditions.

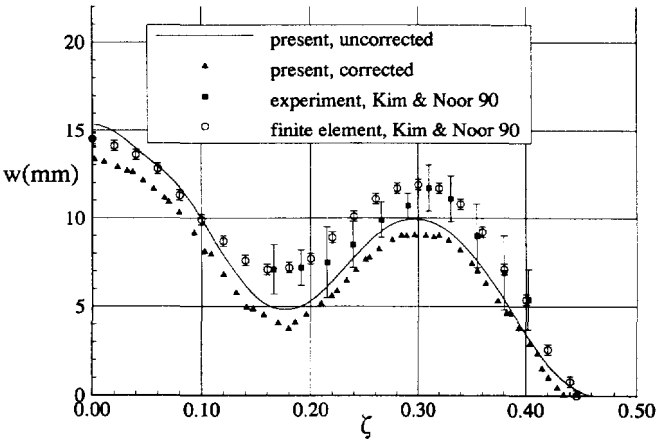

Fig. 17. Finite element calculations compared to experimental (measured) values for space shuttle nose-wheel tire. See text for discussion of error bars.

are fixed at the tire/rim interfaces (see Fig. 16). A convergence tolerance of $10^{-4}\%$ was used in the analysis, and the inflation loads were applied in six equal increments. The pressure vector directions were not updated in this portion of the study. The results of the inflation study are depicted in Fig. 17. The "uncorrected" deflection represents the deflection of the reference surface, which, ignoring any thickness change, is also the displacement of the outer surface. The "corrected" data points adjust these displacements for thickness stretching, Δh, by numerically integrating the strain, $B_{33}(z)$, from the reference surface to the outer surface at each Gauss point. That is,

$$\Delta h = \int_0^{z_{N+1}} B_{33}(z)\,\mathrm{d}z. \tag{64}$$

The error bars on the experimental data have two sources: (1) the measured radial displacement at a given meridional location may have slightly different values at different circumferential locations and the error bars encompass that variation, and (2) precision error is introduced in reading the graphical data from the plots of the work of Kim and Noor (1990). In any case, the calculated displacements are clearly less than the experimental ones. Two possible sources of this difference are (1) any finite element solution should be somewhat stiffer than its "real" counterpart, and (2) the present analysis models no viscoelastic properties. It is likely that the tire material exhibits some "creep" after inflation and, depending upon when the measurements were taken, these time-dependent properties may have influenced the result (according to DeEskinazi *et al.*, 1978, the majority of this creep occurs shortly after inflation).

It is important to recall that the finite element formulation calculates the thickness stretching based upon the assumption of zero stress at the boundaries. For the tire inflation

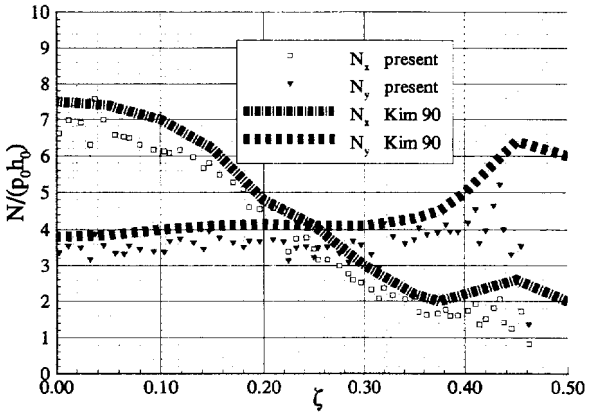

Fig. 18. Finite element stress resultants compared to finite element calculations of Kim and Noor (1990).

problem, this assumption is patently false. However, the thickness change calculated by the model, generated by the membrane stretching due to application of equivalent nodal loads, provides good results in predicting the displaced outer surface of the tire.

Stress resultants for the finite element results are calculated by integrating the stresses through the thickness:

$$N_x = \int_{z_1}^{z_{N+1}} J_{11}(z)\,dz, \quad N_y = \int_{z_1}^{z_{N+1}} J_{22}(z)\,dz, \quad N_z = \int_{z_1}^{z_{N+1}} J_{33}(z)\,dz, \tag{65a}$$

$$N_{xy} = \int_{z_1}^{z_{N+1}} J_{12}(z)\,dz, \quad N_{xz} = \int_{z_1}^{z_{N+1}} J_{13}(z)\,dz, \quad N_{yz} = \int_{z_1}^{z_{N+1}} J_{23}(z)\,dz. \tag{65b}$$

They are then nondimensionalized by dividing by the inflation pressure, $p_0 = 2.206$ MPa (320 psi), and the tire thickness at the crown, $h_0 = 19.05$ mm (0.75 in). The resultants generated by the finite element model are shown in Fig. 18. They are compared with the results of the finite element model of Kim and Noor (1990), who used a semi-analytic finite element model employing moderate-rotation Sanders–Budiansky shell theory and having the following properties: (1) the shell variables are represented by Fourier series in the circumferential direction and piecewise polynomials in the meridional direction, and (2) the fundamental unknowns in the model are strain–resultant parameters, stress–resultant parameters, and generalized displacements. The line thickness in the plot reflects the imprecision in reading the graphical data. As stress–resultants are a fundamental unknown in the model, it is likely that the values of Kim and Noor in Fig. 18 are more reliable than those of the present research, in which the stresses are tertiary quantities calculated from strains generated by displacements. Still, the agreement between solutions is good, except near the tire/rim interface. In this region, the element thicknesses are changing rapidly, causing erratic results. This is due to the discontinuity introduced by having different ply lay-ups adjacent to each other at nodes. Consider Fig. 19, which depicts the effect of this difference. Recall that the displacements away from the shell reference surface are determined by enforcing stress and displacement continuity at interlaminar boundaries. Therefore, the element configuration (number, angles, thicknesses, and constitutive properties of the plys) and the displacements at the reference surface uniquely determine the values of these through-the-thickness displacements. If two adjacent elements have identical configurations (Case $(A) \rightarrow (B)$ of Fig. 19), then the displacement conditions at their common node(s) on the reference surface will determine the displacements away from the reference surface at the node. Furthermore, these displacements will be identical at the node whether it is approached from the element on the left or the right. On the contrary, if the adjacent elements have different configurations (Case $(C) \rightarrow (D)$ of Fig. 19) then, while the displacements at the common node(s) on the reference surface are unique, the difference in

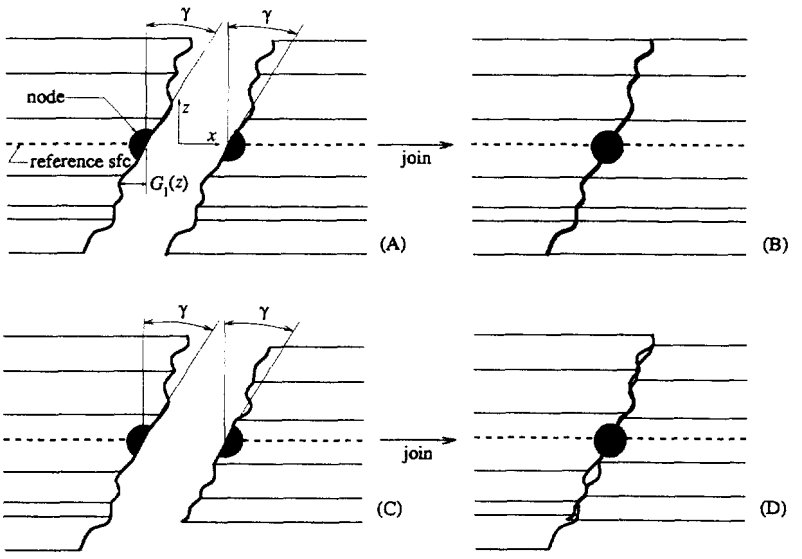

Fig. 19. Discontinuity introduced by adjacent elements of different ply lay-up; Case $(A) \rightarrow (B)$: adjacent elements of identical configuration; Case $(C) \rightarrow (D)$: adjacent elements of different configuration.

Table 1. Maximum stresses and strains due to inflation of the shuttle tire model without pressure direction updates

Component (ij)	11	22	33	12	23	13
Stress J_{ij} (MPa)	36.91	27.76	4.022	27.428	−0.5976	0.2121
Occurs in element	16	10	3	10	10	11
Distance from ref. sfc (z mm)	−0.8255	−0.5135	−15.93	−0.5135	0.5135	0.0
Strain B_{ij} (%)	4.131	23.642	−55.25	−1.696	−25.01	13.212
Occurs in element	16	16	16	3	12	10
Distance from ref. sfc (z mm)	+7.247	+7.247	+4.128	−18.41	−0.5745	−0.5135

element configuration will cause a mismatch in the displacement functions through-the-thickness. The effect of the mis-match is to cause a discontinuity in the strain energy along interelement boundaries (since integration through the thickness is included in that calculation). In qualitative terms, it should be clear that very gradual changes in element properties are more desirable than sudden ones.

The peak stresses in the inflated tire are noted in Table 1. The element numbers in the table correspond to those used in Fig. 14. The largest strains in Table 1 are located in the outer ply which is isotropic rubber. It has a modulus roughly two orders of magnitude less than that of the nylon-corded rubber of the other plys. The maximum transverse normal strain of $B_{33\max} = -55\%$ is large, but is on the order of that seen by Simo *et al.* (1990) in finite element modeling of a transversely loaded rubber sphere. In that instance, strains of 55% were seen.

Another source of the erratic results near the tire/wheel interface is that the current (displacement based) model imposes a fully-clamped boundary condition at the rim, while the stress–resultant parameters used by Kim and Noor (1990) permit non-zero stresses in the interface region. In this displacement-based scheme, the setting of the displacements in the clamped regions to zero has the result of setting strains to zero and therefore stresses to zero. In contrast, when stress–resultant parameters are used as fundamental unknowns (as opposed to a derived quantity) they need not be *a priori* set to zero along a clamped boundary.

8. CONCLUSION

The complex geometry of the tire presents a formidable challenge to describing its behavior with two-dimensional finite elements. In this paper, a two-dimensional finite

element model which includes both layer-wise higher-order transverse shear and thickness stretching is applied to the space shuttle nose gear tire. The two-dimensional element successfully generates a quasi-three-dimensional response through: (1) representation of the reference surface by the tension spline technique, (2) modeling the continuously changing (in the meridional direction) properties of the tire with a discontinuously changing finite element representation of the tire, (3) modeling behavior away from the reference surface through layer-wise polynomial representations of shear warping and thickness stretching, and (4) applying inflation loads at nodes on the reference surface using equivalent nodal loads. Despite the fact that the thickness stretch functions assume no normal stresses on the inner surface of the tire, the inflated tire profile, corrected for thickness stretch, represents the measured profile of Kim and Noor (1990) well. Current and future work will investigate tire contact using this model, including both static footprint and dynamic (rolling) cases.

Acknowledgements—The authors gratefully acknowledge the sponsorship of Dr Arje Nachman and the Air Force Office of Scientific Research, and of Dr Arnold Mayer and the Vehicle Subsystems Division, Flight Dynamics Directorate, Wright Laboratories (USAF). The authors are also grateful for the many helpful conversations with P. Frank Pai of North Carolina A&T University.

REFERENCES

Atluri, S. N. (1984). Alternate stress and conjugate strain measures, and mixed variational formulations involving rigid rotations, for computational analyses of finitely deformed solids, with applications to plates and shells—I, theory, *Computers and Structures* **18,** 93–116.

Atluri, S. N. and Murkawa, H. (1977). On hybrid finite element models in nonlinear mechanics. *Finite Elements in Nonlinear Mechanics: Papers Presented at the International Conference on Finite Elements in Nonlinear Solid and Structural Mechanics* (ed. P. G. B. *et al.*) Trondheim, Norway, pp. 3–41.

Bhimaraddi, A. (1984). A higher order theory for free vibration analysis of circular cylindrical shells. *International Journal of Solids and Structures* **20,** 623–630.

Brockman, R. A., Braisted, W. R., Padovan, J., Tabaddor, F. and Clark, S. K. (1992). Design and analysis of aircraft tires. Final report WL-TR-91-3060, Flight Dynamics Directorate, Wright Laboratory, Air Force Systems Command, Wright-Patterson AFB, OH.

Clark, S. K. (ed.) (1981). *Mechanics of Pneumatic Tires*, U.S. Department of Transportation, Washington: DC.

Cook, R. D., Malkus, D. S. and Plesha, M. E. (1989). *Concepts and Applications of Finite Element Analysis*, John Wiley and Sons, NY.

Danielson, D. A. and Hodges, D. H. (1987). Nonlinear beam kinematics by decomposition of the rotation tensor. *Journal of Engineering Mechanics* **54,** 258–262.

DeEskinazi, J., Yang, T. Y. and Soedel, W. (1978). Displacements and stresses resulting from contact of a steel belted radial tire with a flat surface. *Tire Science and Technology* **11,** 48–70.

Epstein, M. and Glockner, P. G. (1977). Nonlinear analysis of multilayered shells. *International Journal of Solids and Structures* **13,** 1081–1089.

Epstein, M. and Huttelmaier, H.-P. (1983). A finite element formulation for multilayered and thick plates. *Computers and Structures* **16,** 645–650.

Eringen, A. C. (1967). *Mechanics of Continua*, John Wiley and Sons, Inc, NY.

Fraeijs de Veubeke, B. (1972). A new variational principle for finite elastic displacements. *International Journal of Engineering Science* **10,** 745–763.

Greer, Jr., J. M. (1996). Non-linear finite element analyses of composite shells by total Lagrangian decomposition with application to the aircraft tire. Ph.D. dissertation, AFIT/DS/ENY/96-1, Graduate School of Engineering, The Air Force Institute of Technology, Wright-Patterson AFB, OH.

Hinrichsen, R. L. and Palazotto, A. N. (1986). Nonlinear finite element analysis of thick composite plates using cubic spline functions. *AIAA Journal* **24,** 1836–1842.

Kennedy, R. and Padovan, J. (1987). Finite element analysis of steady and transiently moving/rolling nonlinear viscoelastic structure—II. Shell and three-dimensional simulations. *Computers and Structures* **27,** 259–273.

Kim, K. O. and Noor, A. K. (1990). Modeling and analysis of the space shuttle nose-gear tire with semianalytic finite elements. NASA Technical Paper TP-2977, NASA, U.S.A.

Kovařík, V. (1980). Cylindrical orthotropic sandwich-type shells under general loading. *Acta Technica ČSAV* **4,** 499–518.

Malvern, L. E. (1969). *Introduction of the Mechanics of a Continuous Medium*, Prentice-Hall, Inc, Englewood Cliffs, NJ.

Meirovitch, L. (1967). *Analytical Methods in Vibrations*, Macmillan, NY.

Mindlin, R. D. (1951). Influence of rotatory inertia and shear on flexural motions of isotropic, elastic plates. *Journal of Applied Mechanics* **18,** 31–38.

Murakami, H. (1984). Laminated composite plate theories with improved inplane responses. In *ASME Pressure Vessels and Piping Conference*, pp. 257–263.

Owen, D. R. J. and Hinton, E. (1980). *Finite Elements in Plasticity: Theory and Practice*, Pineridge Press, Ltd, Swansea, U.K.

Padovan, J. (1975). Traveling waves vibrations and buckling of rotating anisotropic shells of revolution by finite elements. *International Journal of Solids and Structures* **11,** 1367–1380.

Padovan, J. (1976). On viscoelasticity and standing waves in tires. *Tire Science and Technology* **4,** 233–246.

Padovan, J. (1977). Circumferentially traveling radial loads on rings and cylinders. *International Journal of Non-Linear Mechanics* **12,** 241–250.
Pai, P. F. (1995). A new look at shear correction factors and warping functions of anisotropic laminates. *International Journal of Solids and Structures* **32,** 2295–2313.
Pai, P. F. and Nayfeh, A. H. (1992). A nonlinear composite shell theory. *Nonlinear Dynamics* **3,** 431–463.
Pai, P. F. and Nayfeh, A. H. (1994). A new method for the modeling of geometric nonlinearities in structures. *Computers and Structures* **53,** 877–895.
Pai, P. F. and Palazotto, A. N. (1995a). Nonlinear displacement-based finite-element analyses of composite shells—a new total Lagrangian formulation. *International Journal of Solids and Structures* **32,** 3047–3073.
Pai, P. F. and Palazotto, A. N. (1995b). Polar decomposition theory in nonlinear analyses of solids and structures. *Journal of Engineering Mechanics* **121,** 568–581.
Palazotto, A. N. and Dennis, S. T. (1992). *Nonlinear Analyses of Shell Structures*, AIAA Educational Series, American Institute of Aeronautics and Astronautics, Inc, Washington, DC.
Reddy, J. N. (1984). A simple higher-order theory for laminated composite plates. *Journal of Applied Mechanics* **51,** 745–752.
Reddy, J. N. (1989). On refined computational models of composite laminates. *International Journal of Numerical Methods in Engineering* **27,** 361–382.
Reddy, J. N. and Liu, C. F. (1985). A higher order shear deformation theory of laminated composite shells. *International Journal of Engineering Science* **23**(3), 319–330.
Reissner, E. (1945). The effect of transverse shear deformation on the bending of elastic plates. *Journal of Applied Mechanics* **67,** A-69–A-77.
Reissner, E. (1947). On bending of elastic plates. *Quarterly Applied Mathematics* **5,** 55–68.
Renka, R. J. (1987). Interpolatory tension splines with automatic selection of tension factors. *Siam Journal of Scientific and Statistical Computing* **8,** 393–415.
Schimmels, S. A. and Palazotto, A. N. (1994). Nonlinear geometric and material behavior of shell structures with large strains. *Journal of Engineering Mechanics* **120,** 320–345.
Simo, J. C., Fox, D. D. and Rifai, M. S. (1990). On a stress resultant geometrically exact shell model. Part III. Computational aspects of the nonlinear theory. *Computer Methods in Applied Mechanical Engineering* **79,** 21–70.
Strang, G. (1988). *Linear Algebra and Its Applications*, Harcourt Brace Jovanovich, San Diego.
Sve, C. and Herrmann, G. (1974). Moving load on a laminated composite. *Journal of Applied Mechanics* **41**(3), 663–667.
Truesdell, C. and Toupin, R. A. (1960). The classical field theories. In *Encyclopedia of Physics*, Volume 3/1 (ed. S. Flügge), Springer-Verlag, Berlin.
Washizu, K. (1982). *Variational Methods in Elasticity and Plasticity* (third edn.), Pergamon Press, Oxford.
Whitney, J. M. (1987). *Structural Analysis of Laminated Anisotropic Plates*, Technomic Publishing, Inc, Lancaster, PA.
Wu, B. and Du, X. (1995). Finite element formulation of radial tires with variable constraint conditions. *Computers and Structures* **55,** 871–875.

APPENDIX: MATERIAL PROPERTIES

This appendix lists the material properties used in the finite element inflation problem. The following conventions are employed:

1. Ply numbering is from bottom (inner surface) to top (outer surface)
2. Angle θ is measured from the x (circumferential) axis
3. Coordinate z represents the location of the bottom of the ith ply (z_i), and coordinate z_1 represents the location of the top of the ply (z_{i+1}).
4. The element configuration numbers describe the configuration for an entire (circumferential) row of elements, numbered from the tire/rim interface to the crown. For example, element configuration 16 is the configuration for the two rows of elements at the tire crown (see Fig. 14).

Calculations of the various material properties were based upon the data provided in the reference by Kim and Noor (1990), which contains a very complete description of the material properties and geometry of this tire.

A comment is in order regarding the Poisson's ratio used for nylon-corded rubber properties. As pointed out by Brockman *et al.* (1992), the Poisson's ratio of the nylon cord reflects its structural behavior in tension: that of twisting as well as contraction (Clark, 1981). In light of this, the fact that the values exceed the theoretical limit of 1/2 should not be considered unusual.

Element configuration 1 ($\zeta = 0.5$, the tire/rim interface)

ply	θ°	z	z_1	t	E_{11}	E_{22}	E_{33}	ν_{12}	ν_{23}	ν_{13}	G_{12}	G_{23}	G_{13}
1	0.0	−39.89	−36.93	2.96	3.1	3.1	3.1	0.49	0.49	0.49	1.0	1.0	1.0
2	−51.0	−36.93	−35.83	1.1	469.2	5.3	5.3	0.523	0.66	0.523	1.3	0.8	1.3
3	51.0	−35.83	−34.73	1.1	469.2	5.3	5.3	0.523	0.66	0.523	1.3	0.8	1.3
4	−57.0	−34.73	−33.2	1.53	424.2	5.1	5.1	0.52	0.66	0.52	1.3	0.8	1.3
5	57.0	−33.2	−31.67	1.53	424.2	5.1	5.1	0.52	0.66	0.52	1.3	0.8	1.3
6	0.0	−31.67	−25.4	6.27	2×10^5	2×10^5	2×10^5	0.3	0.3	0.3	76900.0	76900.0	76900.0
7	57.0	−25.4	−23.87	1.54	424.2	5.1	5.1	0.52	0.66	0.52	1.3	0.8	1.3
8	−57.0	−23.87	−22.33	1.53	424.2	5.1	5.1	0.52	0.66	0.52	1.3	0.8	1.3
9	57.0	−22.33	−20.8	1.53	424.2	5.1	5.1	0.52	0.66	0.52	1.3	0.8	1.3
10	−57.0	−20.8	−19.27	1.53	424.2	5.1	5.1	0.52	0.66	0.52	1.3	0.8	1.3
11	0.0	−19.27	−13.0	6.27	2×10^5	2×10^5	2×10^5	0.3	0.3	0.3	76900.0	76900.0	76900.0

12	−57.0	−13.0	−11.46	1.53	424.2	5.1	5.1	0.52	0.66	0.52	1.3	0.8	1.3
13	57.0	−11.46	−9.93	1.53	424.2	5.1	5.1	0.52	0.66	0.52	1.3	0.8	1.3
14	−57.0	−9.93	−7.77	2.16	301.9	4.4	4.4	0.511	0.66	0.511	1.2	0.7	1.2
15	57.0	−7.77	−5.61	2.16	301.9	4.4	4.4	0.511	0.66	0.511	1.2	0.7	1.2
16	0.0	−5.61	5.61	11.21	3.1	3.1	3.1	0.49	0.49	0.49	1.0	1.0	1.0

Element configuration 2

ply	θ°	z	z_1	t	E_{11}	E_{22}	E_{33}	ν_{12}	ν_{23}	ν_{13}	G_{12}	G_{23}	G_{13}
1	0.0	−26.63	−23.75	2.88	3.1	3.1	3.1	0.49	0.49	0.49	1.0	1.0	1.0
2	−51.0	−23.75	−22.76	0.99	518.0	5.6	5.6	0.526	0.66	0.526	1.4	0.8	1.4
3	51.0	−22.76	−21.76	0.99	518.0	5.6	5.6	0.526	0.66	0.526	1.4	0.8	1.4
4	−57.0	−21.76	−20.38	1.39	468.2	5.3	5.3	0.523	0.66	0.523	1.3	0.8	1.3
5	57.0	−20.38	−18.98	1.39	468.2	5.3	5.3	0.523	0.66	0.523	1.3	0.8	1.3
6	0.0	−18.98	−13.31	5.67	2×10^5	2×10^5	2×10^5	0.3	0.3	0.3	76900.0	76900.0	76900.0
7	57.0	−13.31	−11.92	1.39	468.2	5.3	5.3	0.523	0.66	0.523	1.3	0.8	1.3
8	−57.0	−11.92	−10.53	1.39	468.2	5.3	5.3	0.523	0.66	0.523	1.3	0.8	1.3
9	57.0	−10.53	−9.15	1.39	468.2	5.3	5.3	0.523	0.66	0.523	1.3	0.8	1.3
10	−57.0	−9.15	−7.76	1.39	468.2	5.3	5.3	0.523	0.66	0.523	1.3	0.8	1.3
11	0.0	−7.76	−2.08	5.67	2×10^5	2×10^5	2×10^5	0.3	0.3	0.3	76900.0	76900.0	76900.0
12	−57.0	−2.08	−0.69	1.39	468.2	5.3	5.3	0.523	0.66	0.523	1.3	0.8	1.3
13	57.0	−0.69	0.69	1.39	468.2	5.3	5.3	0.523	0.66	0.523	1.3	0.8	1.3
14	−57.0	0.69	2.65	1.96	333.2	4.6	4.6	0.513	0.66	0.513	1.2	0.7	1.2
15	57.0	2.65	4.61	1.96	333.2	4.6	4.6	0.513	0.66	0.513	1.2	0.7	1.2
16	0.0	4.61	8.47	3.86	3.1	3.1	3.1	0.49	0.49	0.49	1.0	1.0	1.0

Element configuration 3

ply	θ°	z	z_1	t	E_{11}	E_{22}	E_{33}	ν_{12}	ν_{23}	ν_{13}	G_{12}	G_{23}	G_{13}
1	0.0	−18.41	−15.93	2.48	3.1	3.1	3.1	0.49	0.49	0.49	1.0	1.0	1.0
2	−51.0	−15.93	−14.8	1.13	456.3	5.2	5.2	0.522	0.66	0.522	1.3	0.8	1.3
3	51.0	−14.8	−13.68	1.13	456.3	5.2	5.2	0.522	0.66	0.522	1.3	0.8	1.3
4	−57.0	−13.68	−12.07	1.61	433.3	5.1	5.1	0.52	0.66	0.52	1.3	0.8	1.3
5	57.0	−12.07	−10.46	1.61	433.3	5.1	5.1	0.52	0.66	0.52	1.3	0.8	1.3
6	57.0	−10.46	−8.85	1.61	433.3	5.1	5.1	0.52	0.66	0.52	1.3	0.8	1.3
7	−57.0	−8.85	−7.24	1.61	433.3	5.1	5.1	0.52	0.66	0.52	1.3	0.8	1.3
8	57.0	−7.24	−5.63	1.61	433.3	5.1	5.1	0.52	0.66	0.52	1.3	0.8	1.3
9	−57.0	−5.63	−4.02	1.61	433.3	5.1	5.1	0.52	0.66	0.52	1.3	0.8	1.3
10	57.0	−4.02	−2.41	1.61	433.3	5.1	5.1	0.52	0.66	0.52	1.3	0.8	1.3
11	−57.0	−2.41	−0.8	1.61	433.3	5.1	5.1	0.52	0.66	0.52	1.3	0.8	1.3
12	57.0	−0.8	0.8	1.61	433.3	5.1	5.1	0.52	0.66	0.52	1.3	0.8	1.3
13	−57.0	0.8	2.41	1.61	433.3	5.1	5.1	0.52	0.66	0.52	1.3	0.8	1.3
14	−57.0	2.41	4.51	2.1	311.2	4.5	4.5	0.512	0.66	0.512	1.2	0.7	1.2
15	57.0	4.51	6.61	2.1	311.2	4.5	4.5	0.512	0.66	0.512	1.2	0.7	1.2
16	0.0	6.61	8.49	1.88	3.1	3.1	3.1	0.49	0.49	0.49	1.0	1.0	1.0

Element configuration 4

ply	θ°	z	z_1	t	E_{11}	E_{22}	E_{33}	ν_{12}	ν_{23}	ν_{13}	G_{12}	G_{23}	G_{13}
1	0.0	−16.08	−13.92	2.16	3.1	3.1	3.1	0.49	0.49	0.49	1.0	1.0	1.0
2	−51.0	−13.92	−12.94	0.98	522.2	5.6	5.6	0.527	0.66	0.527	1.4	0.8	1.4
3	51.0	−12.94	−11.95	0.98	522.7	5.6	5.6	0.527	0.66	0.527	1.4	0.8	1.4
4	−57.0	−11.95	−10.54	1.41	495.4	5.5	5.5	0.525	0.66	0.525	1.4	0.8	1.4
5	57.0	−10.54	−9.14	1.41	495.4	5.5	5.5	0.525	0.66	0.525	1.4	0.8	1.4
6	57.0	−9.14	−7.73	1.41	495.4	5.5	5.5	0.525	0.66	0.525	1.4	0.8	1.4
7	−57.0	−7.73	−6.33	1.41	495.4	5.5	5.5	0.525	0.66	0.525	1.4	0.8	1.4
8	57.0	−6.33	−4.92	1.41	495.4	5.5	5.5	0.525	0.66	0.525	1.4	0.8	1.4
9	−57.0	−4.92	−3.52	1.41	495.4	5.5	5.5	0.525	0.66	0.525	1.4	0.8	1.4
10	57.0	−3.52	−2.11	1.41	495.2	5.5	5.5	0.525	0.66	0.525	1.4	0.8	1.4
11	−57.0	−2.11	−0.7	1.41	495.4	5.5	5.5	0.525	0.66	0.525	1.4	0.8	1.4
12	57.0	−0.7	0.7	1.41	495.4	5.5	5.5	0.525	0.66	0.525	1.4	0.8	1.4
13	−57.0	0.7	2.11	1.41	495.4	5.5	5.5	0.525	0.66	0.525	1.4	0.8	1.4
14	−57.0	2.11	3.94	1.83	355.9	4.7	4.7	0.515	0.66	0.515	1.3	0.8	1.3
15	57.0	3.94	5.77	1.83	355.9	4.7	4.7	0.515	0.66	0.515	1.3	0.8	1.3
16	0.0	5.77	7.92	2.15	3.1	3.1	3.1	0.49	0.49	0.49	1.0	1.0	1.0

Element configuration 5

ply	θ°	z	z_1	t	E_{11}	E_{22}	E_{33}	ν_{12}	ν_{23}	ν_{13}	G_{12}	G_{23}	G_{13}
1	0.0	−12.54	−10.7	1.84	3.1	3.1	3.1	0.49	0.49	0.49	1.0	1.0	1.0
2	−51.0	−10.7	−9.86	0.84	610.6	6.2	6.2	0.533	0.66	0.533	1.4	0.9	1.4
3	51.0	−9.86	−9.02	0.84	610.6	6.2	6.2	0.533	0.66	0.533	1.4	0.9	1.4
4	−57.0	−9.02	−7.81	1.2	578.9	6.0	6.0	0.531	0.66	0.531	1.4	0.9	1.4
5	57.0	−7.81	−6.61	1.2	579.0	6.0	6.0	0.531	0.66	0.531	1.4	0.9	1.4
6	57.0	−6.61	−5.41	1.2	578.9	6.0	6.0	0.531	0.66	0.531	1.4	0.9	1.4
7	−57.0	−5.41	−4.21	1.2	578.9	6.0	6.0	0.531	0.66	0.531	1.4	0.9	1.4
8	57.0	−4.21	−3.01	1.2	578.9	6.0	6.0	0.531	0.66	0.531	1.4	0.9	1.4
9	−57.0	−3.01	−1.8	1.2	578.9	6.0	6.0	0.531	0.66	0.531	1.4	0.9	1.4
10	57.0	−1.8	−0.6	1.2	578.8	6.0	6.0	0.531	0.66	0.531	1.4	0.9	1.4

11	−57.0	−0.6	0.6	1.2	578.9	6.0	6.0	0.531	0.66	0.531	1.4	0.9	1.4
12	57.0	0.6	1.8	1.2	578.9	6.0	6.0	0.531	0.66	0.531	1.4	0.9	1.4
13	−57.0	1.8	3.0	1.2	578.9	6.0	6.0	0.531	0.66	0.531	1.4	0.9	1.4
14	−57.0	3.0	4.57	1.57	415.9	5.0	5.0	0.519	0.66	0.519	1.3	0.8	1.3
15	57.0	4.57	6.13	1.56	415.9	5.0	5.0	0.519	0.66	0.519	1.3	0.8	1.3
16	0.0	6.13	7.66	1.53	3.1	3.1	3.1	0.49	0.49	0.49	1.0	1.0	1.0

Element configuration 6

ply	θ°	z	z_1	t	E_{11}	E_{22}	E_{33}	ν_{12}	ν_{23}	ν_{13}	G_{12}	G_{23}	G_{13}
1	0.0	−8.63	−7.11	1.52	3.1	3.1	3.1	0.49	0.49	0.49	1.0	1.0	1.0
2	−51.0	−7.11	−6.33	0.78	691.0	6.8	6.8	0.539	0.66	0.539	1.5	0.9	1.5
3	51.0	−6.33	−5.56	0.78	691.9	6.8	6.8	0.539	0.66	0.539	1.5	0.9	1.5
4	−57.0	−5.56	−4.55	1.01	734.1	7.1	7.1	0.542	0.66	0.542	1.5	0.9	1.5
5	57.0	−4.55	−3.54	1.01	734.1	7.1	7.1	0.542	0.66	0.542	1.5	0.9	1.5
6	−57.0	−3.54	−2.52	1.01	733.8	7.1	7.1	0.542	0.66	0.542	1.5	0.9	1.5
7	57.0	−2.52	−1.52	1.01	734.1	7.1	7.1	0.542	0.66	0.542	1.5	0.9	1.5
8	−57.0	−1.52	−0.51	1.01	734.1	7.1	7.1	0.542	0.66	0.542	1.5	0.9	1.5
9	57.0	−0.51	0.51	1.01	734.1	7.1	7.1	0.542	0.66	0.542	1.5	0.9	1.5
10	57.0	0.51	1.52	1.01	734.1	7.1	7.1	0.542	0.66	0.542	1.5	0.9	1.5
11	−57.0	1.52	2.52	1.01	734.1	7.1	7.1	0.542	0.66	0.542	1.5	0.9	1.5
12	−57.0	2.52	4.18	1.66	392.7	4.9	4.9	0.518	0.66	0.518	1.3	0.8	1.3
13	57.0	4.18	5.84	1.66	392.7	4.9	4.9	0.518	0.66	0.518	1.3	0.8	1.3
14	0.0	5.84	7.97	2.13	3.1	3.1	3.1	0.49	0.49	0.49	1.0	1.0	1.0

Element configuration 7

ply	θ°	z	z_1	t	E_{11}	E_{22}	E_{33}	ν_{12}	ν_{23}	ν_{13}	G_{12}	G_{23}	G_{13}
1	0.0	−6.05	−4.53	1.52	3.1	3.1	3.1	0.49	0.49	0.49	1.0	1.0	1.0
2	−47.6	−4.53	−3.81	0.72	795.5	7.6	7.6	0.546	0.66	0.546	1.6	1.0	1.6
3	47.6	−3.81	−3.09	0.72	795.5	7.6	7.6	0.546	0.66	0.546	1.6	1.0	1.6
4	−53.6	−3.09	−2.21	0.88	891.0	8.5	8.5	0.553	0.66	0.553	1.7	1.0	1.7
5	53.6	−2.21	−1.33	0.88	891.0	8.5	8.5	0.553	0.66	0.553	1.7	1.0	1.7
6	−53.6	−1.33	−0.44	0.88	891.0	8.5	8.5	0.553	0.66	0.553	1.7	1.0	1.7
7	53.6	−0.44	0.44	0.88	891.0	8.5	8.5	0.553	0.66	0.553	1.7	1.0	1.7
8	−53.6	0.44	1.33	0.88	891.0	8.5	8.5	0.553	0.66	0.553	1.7	1.0	1.7
9	53.6	1.33	2.21	0.88	891.0	8.5	8.5	0.553	0.66	0.553	1.7	1.0	1.7
10	−53.6	2.21	3.64	1.44	549.4	5.8	5.8	0.529	0.66	0.529	1.4	0.8	1.4
11	−53.6	3.64	5.08	1.44	453.0	5.2	5.2	0.522	0.66	0.522	1.3	0.8	1.3
12	53.6	5.08	6.52	1.44	453.0	5.2	5.2	0.522	0.66	0.522	1.3	0.8	1.3
13	0.0	6.52	7.85	1.33	3.1	3.1	3.1	0.49	0.49	0.49	1.0	1.0	1.0

Element configuration 8

ply	θ°	z	z_1	t	E_{11}	E_{22}	E_{33}	ν_{12}	ν_{23}	ν_{13}	G_{12}	G_{23}	G_{13}
1	0.0	−4.49	−2.97	1.52	3.1	3.1	3.1	0.49	0.49	0.49	1.0	1.0	1.0
2	−46.5	−2.97	−2.23	0.74	808.3	7.7	7.7	0.547	0.66	0.547	1.6	1.0	1.6
3	46.5	−2.23	−1.5	0.74	808.3	7.7	7.7	0.547	0.66	0.547	1.6	1.0	1.6
4	−50.5	−1.5	−0.5	1.0	881.0	8.4	8.4	0.552	0.66	0.552	1.7	1.0	1.7
5	50.5	−0.5	0.5	1.0	881.0	8.4	8.4	0.552	0.66	0.552	1.7	1.0	1.7
6	−50.5	0.5	1.5	1.0	881.0	8.4	8.4	0.552	0.66	0.552	1.7	1.0	1.7
7	50.5	1.5	2.5	1.0	881.0	8.4	8.4	0.552	0.66	0.552	1.7	1.0	1.7
8	−50.5	2.5	3.5	1.0	881.0	8.4	8.4	0.552	0.66	0.552	1.7	1.0	1.7
9	50.5	3.5	4.49	1.0	881.0	8.4	8.4	0.552	0.66	0.552	1.7	1.0	1.7
10	−50.5	4.49	5.79	1.3	500.4	5.5	5.5	0.525	0.66	0.525	1.4	0.8	1.4
11	50.5	5.79	7.09	1.3	500.4	5.5	5.5	0.525	0.66	0.525	1.4	0.8	1.4
12	0.0	7.09	8.41	1.31	3.1	3.1	3.1	0.49	0.49	0.49	1.0	1.0	1.0

Element configuration 9

ply	θ°	z	z_1	t	E_{11}	E_{22}	E_{33}	ν_{12}	ν_{23}	ν_{13}	G_{12}	G_{23}	G_{13}
1	0.0	−4.44	−2.92	1.52	3.1	3.1	3.1	0.49	0.49	0.49	1.0	1.0	1.0
2	−41.5	−2.92	−2.2	0.72	821.7	7.9	7.9	0.548	0.66	0.548	1.6	1.0	1.6
3	41.5	−2.2	−1.47	0.72	821.7	7.9	7.9	0.548	0.66	0.548	1.6	1.0	1.6
4	−47.5	−1.47	−0.49	0.98	895.8	8.5	8.5	0.553	0.66	0.553	1.7	1.0	1.7
5	47.5	−0.49	0.49	0.98	895.8	8.5	8.5	0.553	0.66	0.553	1.7	1.0	1.7
6	−47.5	0.49	1.47	0.98	895.9	8.5	8.5	0.553	0.66	0.553	1.7	1.0	1.7
7	47.5	1.47	2.46	0.98	895.7	8.5	8.5	0.553	0.66	0.553	1.7	1.0	1.7
8	−47.5	2.46	3.44	0.98	895.8	8.5	8.5	0.553	0.66	0.553	1.7	1.0	1.7
9	47.5	3.44	4.42	0.98	895.8	8.5	8.5	0.553	0.66	0.553	1.7	1.0	1.7
10	−47.5	4.42	5.7	1.28	509.0	5.6	5.6	0.526	0.66	0.526	1.4	0.8	1.4
11	47.5	5.7	6.97	1.28	509.0	5.6	5.6	0.526	0.66	0.526	1.4	0.8	1.4
12	0.0	6.97	7.86	0.88	3.1	3.1	3.1	0.49	0.49	0.49	1.0	1.0	1.0

Element configuration 10

ply	θ°	z	z_1	t	E_{11}	E_{22}	E_{33}	ν_{12}	ν_{23}	ν_{13}	G_{12}	G_{23}	G_{13}
1	0.0	−4.5	−2.98	1.52	3.1	3.1	3.1	0.49	0.49	0.49	1.0	1.0	1.0
2	−39.1	−2.98	−2.26	0.72	892.8	8.5	8.5	0.553	0.66	0.553	1.7	1.0	1.7
3	39.1	−2.26	−1.54	0.72	892.8	8.5	8.5	0.553	0.66	0.553	1.7	1.0	1.7
4	−45.1	−1.54	−0.51	1.03	924.2	8.8	8.8	0.555	0.66	0.555	1.7	1.0	1.7

5	45.1	−0.51	0.51	1.03	924.2	8.8	8.8	0.555	0.66	0.555	1.7	1.0	1.7
6	−45.1	0.51	1.54	1.03	924.2	8.8	8.8	0.555	0.66	0.555	1.7	1.0	1.7
7	45.1	1.54	2.57	1.03	924.2	8.8	8.8	0.555	0.66	0.555	1.7	1.0	1.7
8	−45.1	2.57	3.59	1.03	924.2	8.8	8.8	0.555	0.66	0.555	1.7	1.0	1.7
9	45.1	3.59	4.62	1.03	924.2	8.8	8.8	0.555	0.66	0.555	1.7	1.0	1.7
10	−45.1	4.62	5.96	1.34	556.1	5.9	5.9	0.529	0.66	0.529	1.4	0.8	1.4
11	45.1	5.96	7.29	1.34	556.1	5.9	5.9	0.529	0.66	0.529	1.4	0.8	1.4
12	0.0	7.29	8.1	0.81	3.1	3.1	3.1	0.49	0.49	0.49	1.0	1.0	1.0

Element configuration 11

ply	θ°	z	z_1	t	E_{11}	E_{22}	E_{33}	ν_{12}	ν_{23}	ν_{13}	G_{12}	G_{23}	G_{13}
1	0.0	−5.77	−4.24	1.52	3.1	3.1	3.1	0.49	0.49	0.49	1.0	1.0	1.0
2	−36.7	−4.24	−3.48	0.76	842.9	8.1	8.1	0.549	0.66	0.549	1.6	1.0	1.6
3	36.7	−3.48	−2.72	0.76	842.9	8.1	8.1	0.549	0.66	0.549	1.6	1.0	1.6
4	−42.7	−2.72	−1.63	1.09	872.5	8.3	8.3	0.551	0.66	0.551	1.7	1.0	1.7
5	42.7	−1.63	−0.54	1.09	872.5	8.3	8.3	0.551	0.66	0.551	1.7	1.0	1.7
6	−42.7	−0.54	0.54	1.09	872.5	8.3	8.3	0.551	0.66	0.551	1.7	1.0	1.7
7	42.7	0.54	1.63	1.09	872.5	8.3	8.3	0.551	0.66	0.551	1.7	1.0	1.7
8	−42.7	0.63	2.72	1.09	872.5	8.3	8.3	0.551	0.66	0.551	1.7	1.0	1.7
9	42.7	2.72	3.81	1.09	872.5	8.3	8.3	0.551	0.66	0.551	1.7	1.0	1.7
10	−42.7	3.81	5.22	1.41	525.2	5.7	5.7	0.527	0.66	0.527	1.4	0.8	1.4
11	42.7	5.22	6.64	1.41	525.2	5.7	5.7	0.527	0.66	0.527	1.4	0.8	1.4
12	0.0	6.64	8.04	1.4	3.1	3.1	3.1	0.49	0.49	0.49	1.0	1.0	1.0

Element configuration 12

ply	θ°	z	z_1	t	E_{11}	E_{22}	E_{33}	ν_{12}	ν_{23}	ν_{13}	G_{12}	G_{23}	G_{13}
1	0.0	−7.15	−5.63	1.52	3.1	3.1	3.1	0.49	0.49	0.49	1.0	1.0	1.0
2	−34.3	−5.63	−4.83	0.8	798.0	7.7	7.7	0.546	0.66	0.546	1.6	1.0	1.6
3	34.3	−4.83	−4.02	0.8	798.0	7.7	7.7	0.546	0.66	0.546	1.6	1.0	1.6
4	−40.3	−4.02	−2.87	1.15	826.4	7.9	7.9	0.548	0.66	0.548	1.6	1.0	1.6
5	40.3	−2.87	−1.72	1.15	826.6	7.9	7.9	0.548	0.66	0.548	1.6	1.0	1.6
6	−40.3	−1.72	−0.57	1.15	826.4	7.9	7.9	0.548	0.66	0.548	1.6	1.0	1.6
7	40.3	−0.57	0.57	1.15	826.4	7.9	7.9	0.548	0.66	0.548	1.6	1.0	1.6
8	−40.3	0.57	1.72	1.15	826.4	7.9	7.9	0.548	0.66	0.548	1.6	1.0	1.6
9	40.3	1.72	2.87	1.15	826.4	7.9	7.9	0.548	0.66	0.548	1.6	1.0	1.6
10	−40.3	2.87	4.37	1.49	497.6	5.5	5.5	0.525	0.66	0.525	1.4	0.8	1.4
11	40.3	4.37	5.86	1.49	497.6	5.5	5.5	0.525	0.66	0.525	1.4	0.8	1.4
12	0.0	5.86	8.05	2.19	3.1	3.1	3.1	0.49	0.49	0.49	1.0	1.0	1.0

Element configuration 13

ply	θ°	z	z_1	t	E_{11}	E_{22}	E_{33}	ν_{12}	ν_{23}	ν_{13}	G_{12}	G_{23}	G_{13}
1	0.0	−8.66	−7.14	1.52	3.1	3.1	3.1	0.49	0.49	0.49	1.0	1.0	1.0
2	−32.4	−7.14	−6.29	0.85	758.5	7.3	7.3	0.543	0.66	0.543	1.6	0.9	1.6
3	32.4	−6.29	−5.45	0.85	757.6	7.3	7.3	0.543	0.66	0.543	1.6	0.9	1.6
4	−38.4	−5.45	−4.24	1.21	784.9	7.5	7.5	0.545	0.66	0.545	1.6	1.0	1.6
5	38.4	−4.24	−3.02	1.21	784.9	7.5	7.5	0.545	0.66	0.545	1.6	1.0	1.6
6	−38.4	−3.02	−1.81	1.21	784.9	7.5	7.5	0.545	0.66	0.545	1.6	1.0	1.6
7	38.4	−1.81	−0.6	1.21	784.9	7.5	7.5	0.545	0.66	0.545	1.6	1.0	1.6
8	−38.4	−0.6	0.6	1.21	784.9	7.5	7.5	0.545	0.66	0.545	1.6	1.0	1.6
9	38.4	0.6	1.81	1.21	784.9	7.5	7.5	0.545	0.66	0.545	1.6	1.0	1.6
10	−38.4	1.81	3.39	1.57	472.8	5.3	5.3	0.523	0.66	0.523	1.3	0.8	1.3
11	38.4	3.39	4.96	1.57	472.8	5.3	5.3	0.523	0.66	0.523	1.3	0.8	1.3
12	0.0	4.96	7.84	2.88	3.1	3.1	3.1	0.49	0.49	0.49	1.0	1.0	1.0

Element configuration 14

ply	θ°	z	z_1	t	E_{11}	E_{22}	E_{33}	ν_{12}	ν_{23}	ν_{13}	G_{12}	G_{23}	G_{13}
1	0.0	−10.29	−8.77	1.52	3.1	3.1	3.1	0.49	0.49	0.49	1.0	1.0	1.0
2	−31.2	−8.77	−7.88	0.89	774.3	7.5	7.5	0.544	0.66	0.544	1.6	0.9	1.6
3	31.2	−7.88	−6.99	0.89	773.4	7.4	7.4	0.544	0.66	0.544	1.6	0.9	1.6
4	−37.2	−6.99	−5.72	1.27	801.8	7.7	7.7	0.546	0.66	0.546	1.6	1.0	1.6
5	37.2	−5.72	−4.45	1.27	801.8	7.7	7.7	0.546	0.66	0.546	1.6	1.0	1.6
6	−37.2	−4.45	−3.18	1.27	801.8	7.7	7.7	0.546	0.66	0.546	1.6	1.0	1.6
7	37.2	−3.18	−1.91	1.27	802.0	7.7	7.7	0.546	0.66	0.546	1.6	1.0	1.6
8	−37.2	−1.91	−0.64	1.27	801.5	7.7	7.7	0.546	0.66	0.546	1.6	1.0	1.6
9	37.2	−0.64	0.64	1.27	802.0	7.7	7.7	0.546	0.66	0.546	1.6	1.0	1.6
10	−37.2	0.64	2.29	1.65	506.2	5.5	5.5	0.526	0.66	0.526	1.4	0.8	1.4
11	37.2	2.29	3.94	1.65	506.2	5.5	5.5	0.526	0.66	0.526	1.4	0.8	1.4
12	−31.2	3.94	5.59	1.65	228.3	4.1	4.1	0.506	0.66	0.506	1.2	0.7	1.2
13	0.0	5.59	7.41	1.82	3.1	3.1	3.1	0.49	0.49	0.49	1.0	1.0	1.0

Element configuration 15

ply	θ°	z	z_1	t	E_{11}	E_{22}	E_{33}	ν_{12}	ν_{23}	ν_{13}	G_{12}	G_{23}	G_{13}
1	0.0	−10.29	−8.77	1.52	3.1	3.1	3.1	0.49	0.49	0.49	1.0	1.0	1.0
2	−30.3	−8.77	−7.88	0.89	774.0	7.5	7.5	0.544	0.66	0.544	1.6	0.9	1.6
3	30.3	−7.88	−6.99	0.89	773.7	7.5	7.5	0.544	0.66	0.544	1.6	0.9	1.6

4	−36.3	−6.99	−5.72	1.27	801.8	7.7	7.7	0.546	0.66	0.546	1.6	1.0	1.6
5	36.3	−5.72	−4.45	1.27	801.8	7.7	7.7	0.546	0.66	0.546	1.6	1.0	1.6
6	−36.3	−4.45	−3.18	1.27	801.8	7.7	7.7	0.546	0.66	0.546	1.6	1.0	1.6
7	36.3	−3.18	−1.91	1.27	802.0	7.7	7.7	0.546	0.66	0.546	1.6	1.0	1.6
8	−36.3	−1.91	−0.64	1.27	801.8	7.7	7.7	0.546	0.66	0.546	1.6	1.0	1.6
9	36.3	−0.64	0.64	1.27	801.8	7.7	7.7	0.546	0.66	0.546	1.6	1.0	1.6
10	−36.3	0.64	2.29	1.65	506.2	5.5	5.5	0.526	0.66	0.526	1.4	0.8	1.4
11	36.3	2.29	3.94	1.65	506.2	5.5	5.5	0.526	0.66	0.526	1.4	0.8	1.4
12	−30.3	3.94	5.59	1.65	228.3	4.1	4.1	0.506	0.66	0.506	1.2	0.7	1.2
13	0.0	5.59	8.31	2.72	3.1	3.1	3.1	0.49	0.49	0.49	1.0	1.0	1.0

Element configuration 16 ($\zeta = 0$, the tire crown)

ply	θ°	z	z_1	t	E_{11}	E_{22}	E_{33}	ν_{12}	ν_{23}	ν_{13}	G_{12}	G_{23}	G_{13}
1	0.0	−11.75	−10.23	1.52	3.1	3.1	3.1	0.49	0.49	0.49	1.0	1.0	1.0
2	−29.8	−10.23	−9.34	0.89	774.3	7.5	7.5	0.544	0.66	0.544	1.6	0.9	1.6
3	29.8	−9.34	−8.45	0.89	773.4	7.4	7.4	0.544	0.66	0.544	1.6	0.9	1.6
4	−35.8	−8.45	−7.18	1.27	801.8	7.7	7.7	0.546	0.66	0.546	1.6	1.0	1.6
5	35.8	−7.18	−5.91	1.27	801.8	7.7	7.7	0.546	0.66	0.546	1.6	1.0	1.6
6	−35.8	−5.91	−4.64	1.27	801.8	7.7	7.7	0.546	0.66	0.546	1.6	1.0	1.6
7	35.8	−4.64	−3.37	1.27	801.8	7.7	7.7	0.546	0.66	0.546	1.6	1.0	1.6
8	−35.8	−3.37	−2.1	1.27	802.0	7.7	7.7	0.546	0.66	0.546	1.6	1.0	1.6
9	35.8	−2.1	−0.83	1.27	801.8	7.7	7.7	0.546	0.66	0.546	1.6	1.0	1.6
10	−35.8	−0.83	0.83	1.65	506.2	5.5	5.5	0.526	0.66	0.526	1.4	0.8	1.4
11	35.8	0.83	2.48	1.65	506.2	5.5	5.5	0.526	0.66	0.526	1.4	0.8	1.4
12	−29.8	2.48	4.13	1.65	228.3	4.1	4.1	0.506	0.66	0.506	1.2	0.7	1.2
13	0.0	4.13	7.25	3.12	3.1	3.1	3.1	0.49	0.49	0.49	1.0	1.0	1.0